Spin-polarized Transport in Nanoelectromechanical Systems

Dissertation zur Erlangung des Doktorgrades
an der Fakultät für Mathematik, Informatik und
Naturwissenschaften
Fachbereich Physik
der Universität Hamburg

vorgelegt von

Jochen Brüggemann

Hamburg, 2015

Gutachter der Dissertation:	Prof. Dr. Michael Thorwart
	Prof. Dr. Jürgen König
Gutachter der Disputation:	Prof. Dr. Daniela Pfannkuche
	Prof. Dr. Michael Thorwart
	Prof. Dr. Jürgen König
	Prof. Dr. Hans Peter Oepen
	Priv.-Doz. Dr. Peter Nalbach
Datum der Disputation:	01.06.2015
Vorsitzender des Prüfungsausschusses:	Prof. Dr. Daniela Pfannkuche

Abstract

In this work, the interplay between vibrational degrees of freedom and spin-polarized charge transport on the nanoscale, induced by ferromagnetic charge reservoirs, is investigated. The dynamics of two different systems is determined by numerically solving the Redfield master equation for the time-evolution of the reduced density matrix in the sequential tunneling limit.

The first system is a proof-of-principle model for a dynamical cooling setup on the nanoscale utilizing magnetomechanical interactions to reduce the vibrational energy of a single phonon mode. The setup consists of a magnetic quantum dot tunnel-coupled to a pair of ferromagnetic leads. Using spin-polarized currents, it is possible to polarize the local magnetic moment of the quantum dot. Magnetomechanical interactions then lead to an exchange of energy between the magnetic and vibrational degrees of freedom, resulting in a decrease of the vibrational energy. The model is compared to recent experiments to analyze its feasibility. The principle mechanism of the cooling protocol is discussed and a meaningful initial preparation of the setup is found. The spin and phonon dynamics of the system are analyzed for three different setups of the lead polarization directions. An anti-parallel alignment of the source and drain lead polarizations is identified as the optimal cooling setup due to an accumulation of spin on the quantum dot. For a wide range of parameters a net cooling effect of the vibrational mode is reported. A maximum of the cooling effect is found as a function of the magnetomechanical coupling. This implies that cooling can be achieved not only for strong magnetomechanical interactions.

The second system is an Anderson-Holstein model coupled to ferromagnetic leads. Here, the differential conductance is determined as a function of the applied bias voltage. The aim of this investigation is to explain experimental observations of the conductance of a Cobalt-Phthalocyanine molecule in a scanning tunneling microscopy setup. The numerical calculation of the conductance for the theory model is able to resolve the main structure of the experimental data. A strong agreement is found for the position of the conductance peaks with respect to the bias voltage. Discrepancies between the theory and the experiment appear when the polarization of the microscope tip is reversed. The change in peak intensities and positions observed in the experiment is not recovered by a numerical calculation. These effects are assumed to originate from the magnetic exchange field induced by the ferromagnetic leads. Due to the numerical restriction to the sequential tunneling and, therefore, to weak system-lead couplings, a direct com-

parison of the influence of the exchange field between the experiment and the theory model is not possible. In the last part of the thesis the effects of non-equilibrium and equilibrium vibrations on the transport properties of the second system are evaluated. A direct comparison shows that non-equilibrium distribution of the phonon mode leads to a qualitative change in the transport dynamics only in the strong bias regime.

Kurzfassung

In dieser Arbeit wird das Zusammenspiel von vibronischen Freiheitsgraden und spinpolarisiertem Ladungstransport auf der Nanoskala, induziert durch ferromagnetische Zuleitungen, untersucht. Die Dynamik von zwei verschiedenen Systemen wird bestimmt durch die Lösung der Redfield Master Gleichung für die Zeitentwicklung der reduzierten Dichtematrix im sequentiellen Tunnellimit.

Das erste System ist ein Model für einen Machbarkeitsnachweis eines dynamischen Kühlmechanismus auf der Nanoskala, der magnetomechanische Wechselwirkungen benutzt, um die vibronische Energie einer einzelnen Phononenmode zu reduzieren. Das Modell besteht aus einem magnetischen Quantenpunkt, der an ein Paar von ferromagnetischen Zuleitungen gekoppelt ist. Durch die Nutzung von spin-polarisierten Strömen ist es möglich, die lokale Magnetisierung des Quantenpunktes zu polarisieren. Magnetomechanische Wechselwirkungen resultieren dann in einem Austausch von Energie zwischen den magnetischen und vibronischen Freiheitsgraden und dadurch in einer Abnahme der vibronischen Energie. Das Modell wird mit aktuellen Experimenten verglichen, um seine Realisierbarkeit zu überprüfen. Der grundlegende Mechanismus des Kühlprotokolls wird diskutiert und eine sinnvolle Präparation des Aufbaus wird gefunden. Die Spin- und Phononendynamik des Systems wird für drei verschiedene Konfigurationen der Polarisierungsrichtungen der ferromagnetischen Zuleitungen analysiert. Durch die Akkumulation von Spins auf dem Quantenpunkt stellt sich die anti-parallele Ausrichtung der Polarisierungen der beiden Zuleitungen als optimale Konfiguration für das Kühlen heraus. Ein Gesamtkühleffekt der vibronischen Freiheitsgrade wird für einen großen Parameterbereich gefunden. Dieser Kühleffekt hat ein Maximum als Funktion der magnetomechanischen Kopplung. Dies bedeutet, dass Kühlung nicht nur für starke magnetomechanische Wechselwirkungen möglich ist.

Das zweite System besteht aus einem Anderson-Holstein Modell gekoppelt an ferromagnetische Zuleitungen. Die differentielle Leitfähigkeit wird als Funktion der Spannung ermittelt. Das Ziel dieser Untersuchung ist die Erklärung experimenteller Messungen für die Leitfähigkeit von Cobalt-Phthalocyanine am Rastertunnelmikroskop. Die numerischen Ergebnisse für die Leitfähigkeit im Theorie-Modell spiegeln die Hauptstrukturen der experimentellen Daten wider. Es wird eine starke Übereinstimmung für die Positionen der Spitzen in der differentiellen Leitfähigkeit gefunden. Unterschiede zwischen der Theorie und dem Experiment treten auf, wenn die Polarisierung der Spitze des Rastertunnelmikroskops umgekehrt wird. Die im Experiment beobachteten Änderungen

der Höhe und Position der Leitfähigkeitshöchstwerte erscheinen nicht in der numerischen Berechnung. Diese Effekte werden auf das Austauschfeld, welches von den ferromagnetischen Zuleitungen induziert wird, zurückgeführt. Aufgrund der Beschränkung der numerischen Methode auf schwache System-Bad Kopplungen ist es nicht möglich, einen direkten Vergleich für den Einfluss des Austauschfeldes zwischen Theorie und Experiment anzustellen. Im letzten Teil dieser Arbeit werden die Effekte von Gleichgewichts- und Nichtgleichgewichtsvibrationen auf die Transporteigenschaften des zweiten Systems untersucht. Ein direkter Vergleich zeigt, dass eine Nichtgleichgewichtsverteilung der Phononenmode nur für starke Spannungen zu einem qualitativen Unterschied in den Transporteigenschaften führt.

Contents

1. Introduction

The study of electronic devices on the micro- and nanoscale plays an important role for the development of future technology. Both the memory capacity as well as the operating speed of modern microelectronics depend on the size of the devices. Most modern electronic hardware is composed of integrated circuits which contain arrays of microtransistors. According to Moore's law [1] the number of transistors per microchip doubles roughly every eighteen months. By now, microchips have already reached sizes of the order of tens of nanometers [2] and the process of miniaturization has slowed down [3]. At this scale, also referred to as the nanoscale, quantum effects may start to influence electronic transport properties. Macroscopic materials contain a large number of particles. A mol of water, for example, weighs 18g and contains $6.022 \cdot 10^{23}$ molecules. The physical properties of macroscopic materials measured in a laboratory therefore are the result of an average over these large numbers of molecules rather than their individual properties. In comparison, devices on the nanoscale contain a much smaller number of molecules. Here, the individual behaviour of even a single molecule can play an important role for the measurement of properties such as conductance or heat capacity. Consequently, the investigation of quantum transport on the nanoscale can become a vital component for the development of new technologies.

A particular example for the development of new devices on the nanoscale is the molecular transistor [4, 5]. It consists of a single molecule in electrical contact with three electrodes. By applying a bias voltage between two of the electrodes and a gate voltage at the third electrode, it is possible to control the charge current flowing through the molecule. In macroscale transistors the manipulation of the gate voltage can lead to an increase or decrease of the current flowing through the transistor. Molecular transistors exhibit a similar behaviour due to electron-electron interactions on the molecule. Strong Coulomb interactions between the electrons can lead to a blockade of the charge current. This concept is known as Coulomb blockade physics [6]. Molecules, however, do not only possess electronic but also vibrational and magnetic degrees of freedom. Interactions between these different degrees of freedom lead to new effects and open new possibilities for the manipulation of electric currents.

A well-known effect of the interaction between electric and vibrational degrees of freedom is the Franck-Condon blockade [7–12]. Here, the coupling between the vibrational motion and the number of charges on a nanodevice can lead to a suppression of the current similar to the Coulomb blockade. Furthermore a signature of each vibronic state

of the system can be found in the current-voltage characteristics [13–17]. An example of a system exhibiting such an effect is a quantum dot embedded in a nanoresonator. Here, electrostatic forces between a gate electrode and electrons on the quantum dot can cause a shift in the equilibrium position of the resonator. This shift in turn changes the electronic transport properties of the device and induces a current blockade. Such a phonon-induced current blockade can be enhanced further by driving the resonator through a mechanical instability [18–21]. Consequently, nanoelectromechanical systems (NEMS) can be used as sensitive detectors for displacement, charge or mass [22]. High quality nanoresonators built of carbon nanotubes or SiO_2 nanobeams are excellent conductors. Their quality factors, given by the inverse eigenfrequency, can reach values of the order of 10^5 [16, 17]. At sufficiently low temperatures these nanoresonators operate in the deep quantum regime where zero-point fluctuations and other properties of quantum mechanical motion could be detected. Further research on NEMS is also carried out with the goal of information storage [23–25] by using molecular switches.

The development of new microscopic memory devices and qubits is also pursued in the field of spintronics [26]. The field of spintronics is based on the study and manipulation of electronic spins in solid state systems. Spin-polarized charge transport through nanodevices can be induced by using ferromagnetic charge reservoirs. Ferromagnetic materials exhibit a different density of states for electrons with different spin orientations. Consequently, applying a bias voltage to a set of ferromagnetic leads coupled to a nanodevice induces a spin-polarized current. The influence of ferromagnetic leads on a nanodevice can be expressed in terms of an effective magnetic field [27–31]. Combining this effect with internal magnetic degrees of freedom of nanodevices has lead to the possibility to construct spin filters or spin valves [32, 33]. A non-collinear orientation of the lead polarizations and external magnetic fields leads to interesting phenomena such as a negative differential conductance as a result of spin accumulation and precession on the nanodevice [28].

While both the Franck-Condon blockade as well as spin-polarized charge transport have been investigated in detail individually, a combination of these two effects has so far not been studied. The focus of this thesis is to combine these two effects and investigate spin-polarized charge transport in nanodevices with vibrational degrees of freedom.

Direct interactions between magnetic degrees of freedom and vibrations, in form of heat, are also investigated in the field of spin caloric transport [34]. Here, effects such as the Spin-Seebeck effect [35] are analyzed in order to understand the interplay between

spin and heat-based transport phenomena. Such an understanding is also of importance for the development of new cooling techniques for micro- and nanodevices. Sending a current through a microchip inevitably leads to Ohmic heating. Many modern devices rely on passive cooling mechanisms in order to remove the produced heat. Commonly, heat is transferred to the environment via a thermal contact between the nanoelectrical device and its supporting structure. The efficiency of such passive heating mechanisms however is limited. The demand for larger processing powers and the increasing number of transistors per microchip will eventually lead to a heating problem. A solution can be found by active cooling protocols. Such active or dynamical cooling mechanisms could also further reduce the size of electronic devices by removing the necessity for spacious cooling equipment. One example for such a nanorefrigerator is the idea to remove heat via an electronic charge current [36, 37].

In this thesis, we propose and analyze a novel cooling mechanism on the nanoscale based on magnetic degrees of freedom [38, 39]. In analogy to the macroscale demagnetization cooling [40], we utilize the exchange of energy between magnetic and vibrational degrees of freedom. More accurately, we analyze the spin and phonon dynamics of a magnetic quantum dot with vibrational degrees of freedom coupled to a set on non-collinearly polarized ferromagnetic leads. Applying a bias voltage between the ferromagnetic leads induces a spin-polarized charge current through the quantum dot. This current leads to a polarization of the localized magnetic moment of the quantum dot. Energy exchange between the magnetic and vibrational degrees of freedom then leads to a decrease in the vibrational energy of the device. Simultaneously the charge current gives rise to Ohmic losses which produce heat. Our investigation shows that it is possible to prepare the setup in such a way that the cooling due to magnetomechanical exchange can overcome the Ohmic heating effects leading to an overall effective cooling of the device. A molecular magnet embedded on a suspended carbon nanotube attached to ferromagnetic charge reservoirs could constitute an experimental realization of our theory model. Here, experimentalists have already found a clear signature of magnetomechanical interaction [41]. Similar effects have been reported for nitrogen vacancies coupled to a SiC cantilever [42, 43].

A different use of spin-polarized currents on the nanoscale can be found in spin-resolved spectroscopy. The investigation and development of single molecule transistors requires knowledge of the electronic, mechanical and magnetic properties of the molecule. The energy spectrum of such a molecule can be detected by spectroscopic methods such as scanning tunneling microscopy. The preparation of measurement sam-

ples however often leads to a hybridization of the molecules. This changes exactly those properties which we want to investigate. Recent studies therefore prepare molecules on insulating substrates in order to avoid hybridization [44–47]. In order to understand the resulting experimental findings, we investigate spin-polarized transport in an Anderson-Holstein model [48, 49]. A comparison between the experimental and theoretical data shows a strong influence of the ferromagnetic leads. The effective field formed by the lead polarizations, however, depends on the electronic energy levels which are shifted by the electron-phonon interaction. Strong electron-phonon couplings can therefore lead to a significant change of not only the electronic but also the magnetic properties of the system. These observations indicate that a negative differential conductance or a Kondo-effect [50] could be induced or enhanced by the vibrational degrees of freedom.

For our calculations of the system dynamics for both the nanorefrigerator and the Anderson-Holstein model we rely on a numerical solution of the master equation. A quantum master equation describes the time evolution of an open quantum system under the influence of an environment such as the ferromagnetic leads used in both models. Numerical solutions for the quantum master equation can be found for example by using the quasi-adiabatic path integral formalism (QUAPI)[51–54]. In QUAPI the time evolution of the system is formulated using a path integral. The influence of the environment can then be integrated out and is contained in the so-called influence functional [55]. Depending on the size of the system such a solution for an exact master equation can be numerically very demanding and lead to long calculation times. The same restrictions apply for a direct integration of the master equation or stochastic methods such as Monte-Carlo simulations. In this thesis, we focus on the regime of weak system-bath interactions and Markovian dynamics. Under these two assumptions the master equation can be transformed into a Redfield master equation. A numerical solution of the Redfield equation can be found by solving the eigenvalue problem for the Redfield tensor. This method is significantly faster than the previously mentioned methods. Methods based on the Redfield equation have been successfully used to investigate transport on the nanoscale [56] including both spin-polarized transport [28, 30, 31] as well as phonon-assisted transport [57, 58] or the calculation of heat currents in quantum refrigerators [59].

The thesis is structured as follows. In Chapter 2 we give an overview over Coulomb blockade physics in single-electron transistors and provide a brief summary of preexisting literature explaining fundamental effects which reappear in the course of the thesis. We then establish the numerical framework for our calculations by deriving the

quantum master equation for open quantum systems in the limit of weak system-bath interactions. Chapter 3 is designated to our main results. We develop a dynamic cooling protocol for a magnetic nanodevice and set up a model for a proof-of principle of the nanocooling scheme. By investigating the spin and phonon dynamics of the model we show that an effective cooling of the vibrational degrees of freedom is possible for a wide range of parameters. An investigation of the influence of ferromagnetic leads on charge transport through molecules can be found in Chapter 4. Here, we compare recent experimental findings to a theory model and provide a qualitative explanation by analytic determination of the polaronic shift and the effective magnetic field of the leads. Finally, we give a summary and conclusion of our results in Chapter 5.

2. Theoretical Background

In this chapter we describe the fundamental physical principles and theoretical tools which appear in this thesis. We start by explaining single-electron transport and Coulomb blockade physics using the example of the single-electron transistor in Section 2.1. Based on the conclusions of this example we review literature on the influence of vibrational and magnetic degrees of freedom on quantum transport in Section 2.2. Our goal is to study a combination of these effects. In order to so we derive a master equation for the time evolution of the density matrix of an open quantum system in Section 2.3. Knowledge over the time evolution of our model system allows us to determine transport properties and the dynamics of electrons, vibrations and spins. We discuss the Redfield approach and diagrammatic perturbation theory as tools for solving the master equation and describe the numerical procedure to obtain a solution.

2.1. Single-Electron Transport

The study of mesoscopic or nanosystems often deals with nonequilibrium transport properties. Such properties are also the focus of this thesis. More specifically, we want to investigate spin-polarized transport in nanodevices. For this, we first need to understand the basic principles of charge transport on the nanoscale. Let us start with a quantum system on the nanoscale coupled to an electronic environment. Such an environment can be provided for example by the macroscopic leads of a nanoelectronic device. These leads act as charge reservoirs and the interaction with the system allows charge carriers, the electrons, to tunnel between the system and the leads. Let us further assume that the coupling between the nanodevice and the leads is weak. The average life-time of a charge state on the nanodevice then is quite long. Changing the state is only possible via a transfer of electrons to or from the leads. The probability for such a charge transfer is directly proportional to the coupling strength between leads and system. Specifically a simultaneous occurrence of several charge transfers is very unlikely for weak couplings. As such the elementary physics of the device can be explained by the rather simple mechanism of single-electron transfers. The most prominent example for such a system is the single-electron transistor [6]. Realizations of such devices can be found in form of single molecules [4, 5] or artificially produced quantum dots [60]. In the following we want to provide a qualitative understanding of the behaviour of single-electron devices in the presence of Coulomb interactions.

A single-electron transistor (SET) is the nanoscale equivalent of a classical transistor.

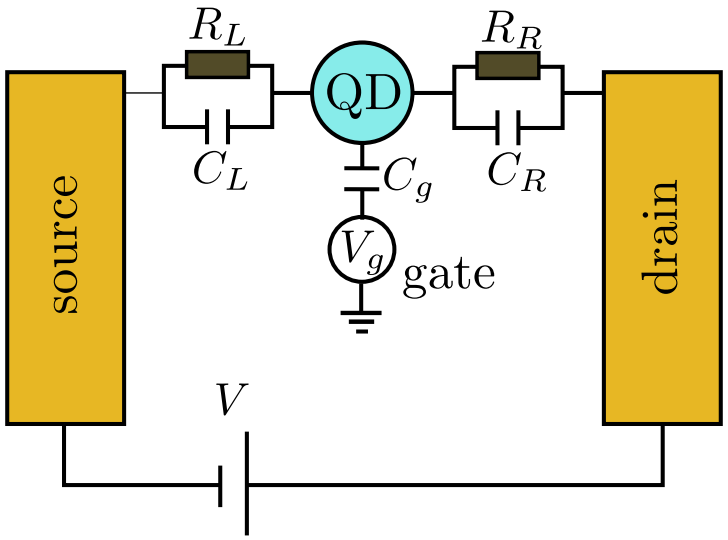

Figure 1: Equivalent circuit of a single-electron transistor consisting of a quantum dot (QD), a source, drain and a gate electrode. In analogy to the classical transistor the charge current flowing through the quantum dot can be controlled by the bias (V) and gate (V_g) voltages.

The classical transistor is a semiconductor device which is used to control and amplify electronic signals and currents. It typically has three terminals called the gate, the source and the drain. Applying a voltage or current to two of these terminals allows us to change the current flowing through a different pair of terminals. Transistors are widely used in integrated circuits for microelectronic devices. The single-electron transistors, whose equivalent circuit is shown in Figure 1, works in a very similar way. Its center is formed by a quantum dot (QD). A quantum dot is a nanostructure with very small spacial dimension therefore exhibiting a discrete energy spectrum. It is often treated as a zero-dimensional object. The quantum dot is connected to three electrodes, the source, the drain and the gate. Tunnel contacts enable charge transport between the dot and the source and drain electrodes. The chemical potential of the latter two can be changed by a bias voltage V. A gate voltage V_g applied to the gate electrode can be used to control the current flowing between source and drain in analogy to the classical transistor. A tunnel barrier prevents a direct charge transport between the gate and the quantum dot.

One of the most interesting features of the single-electron transistor is the Coulomb blockade. It describes a suppression of the current between source and drain voltage

due to strong Coulomb repulsion between electrons on the quantum dot. Many solid state systems have been found to be described surprisingly well within models which neglect electron-electron interactions. Since most of those are many-body systems a full description including such interactions presents an unsolvable problem. To understand, however, experiments on quantum dots these interactions can not be neglected. The small spatial confinement formed by the quantum dot leads to a quantization of the energy spectrum and gives rise to Coulomb repulsion between electrons trapped on the dot. Let us assume that the quantum dot is a point-like structure containing n electrons with charge e. The energy needed to add another electron to the dot is then given by

$$E = \frac{e^2}{2C_\Sigma} n^2 = E_C n^2, \tag{1}$$

where $E_C = e^2/2C_\Sigma$ is the charging energy, $C_\Sigma = C_L + C_R + C_g$ the total capacitance of the single-electron transistor and C_L, C_R and C_g are the capacitances of the source, drain and gate electrode, respectively. As mentioned earlier, the SET can be manipulated by changing the gate and bias voltages. The influence of the electrodes can be expressed as an induced charge $q = C_R V_R + C_L V_L + C_g V_g$, where V_L, V_R denote the potential shift for the source and drain electrode. Notice that the induced charge q is not the charge of a particle and therefore, in contrast to the charge transfer from and to the quantum dot or its occupation number, is not a quantized number. We can then express the energy level of the quantum dot as a function of its occupation number n as

$$E(n) = E_C (n - q/e)^2. \tag{2}$$

Assuming that the quantum dot has no other internal degrees of freedom we have now knowledge of its energy spectrum depending on the number of electrons on the dot and the interaction with the electrodes. Our goal is to discuss single-electron transfers between the quantum dot and the electrodes. A finite current only appears if there is a preferred direction of charge transfer. It can be induced by applying a bias voltage between the source and the drain lead. For simplicity we choose a symmetric bias, $V_L = -V_R = V/2$. There are four different tunneling processes which may appear: transfer of an electron from the source lead onto the quantum dot, from dot to the source lead, from the dot to the drain lead and from the drain lead onto the dot. At zero temperature a charge transfer is only possible if the difference between the initial and final energy of the process is negative. Both the bias voltage as well as the charging

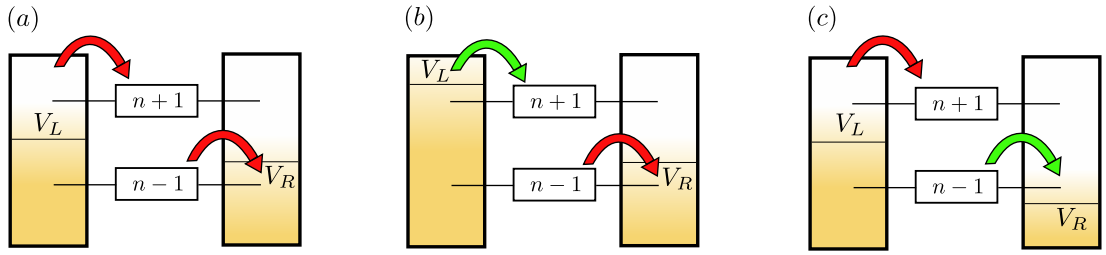

Figure 2: Energy diagram for single-electron transfers in an SET with n electrons occupying the quantum dot. Green arrows signify possible transitions whereas red arrows represent forbidden transitions. In (a) the transport is completely blocked. Adding an additional electron from the source to the QD is possible in (b) and (c) shows the possibility of an electron tunneling from the dot to the drain lead.

energy therefore play an important role in determining whether charge transport is possible or not.

In Figure 2 we illustrate the possibilities for charge transfer in a SET. In (a) all charge transfers are forbidden. This transport regime is known as the Coulomb blockade. The spacing between the energy levels on the quantum dot determined by the charging energy exceeds the bias voltage applied between the source and drain electrode. A blockade is formed and no charge current can flow through the device. The blockade can be lifted by changing the gate or the bias voltage. Electron transport becomes possible if the bias voltage is increased until it exceeds the energy difference between the different charge states. Figure 2 (b) shows an example of such a situation. The chemical potential in the left lead is high enough to allow the transfer of an electron onto the quantum dot therefore changing its charge state from n to $n+1$. If the Fermi level of the drain lead is lower than the next lowest charge state $n-1$, then the transfer of an electron from the QD to the drain is possible as shown in (c). A finite charge current can be observed if both transitions shown in (b) and (c) are possible. Electrons can then successively tunnel through the quantum dot.

An alternative way to change the transport regime is the manipulation of the energy (2) of the device using the gate voltage which changes the induced charge q on the quantum dot. By lowering or raising the energy of all charge states simultaneously, transitions between the leads and the dot can be blocked or allowed. The Coulomb blockade regime can be identified by plotting the conductance of the SET as a function of the induced charge and the bias voltage as shown in Figure 3. Here, the blue regions

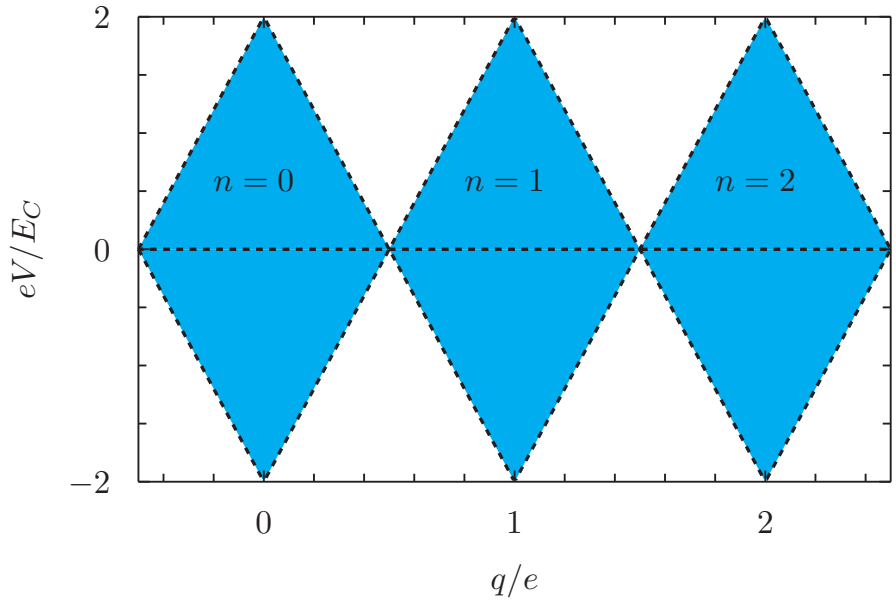

Figure 3: Coulomb diamonds for the single-electron transistor formed by the border between conducting (white) and blocked (blue) regions.

indicate a Coulomb blockade where the conductance of the device vanishes. Analyzing the Coulomb diamonds can yield information about the charge state and the charging energy of the device. Due to the symmetric structure, it is therefore possible to identify the energy as a function of the number of electrons, see Eq. (2), by analyzing only the first two charge states. Additionally, we see that the regime of sequential tunneling of electrons (as in Figure 2 (b) and (c)) also yields the form of a diamond.

So far, we have argued that the current in the Coulomb blockade regime vanishes. Our argument was based on weak system-lead interactions and zero temperature. Finite temperatures, however, induce thermal fluctuations in the energy of the electrons. Previously, we have identified the possibilities for charge transfer by using energy conservation. The energy fluctuations due to finite temperatures now soften these conditions. For this reason, experimental measurements of the Coulomb diamonds can find small but finite currents in the Coulomb blockade regime. There is, however, a second effect which can lead to finite currents in the blocked region. The origin of this effect are cotunneling processes. Even though we have used classical arguments for the charging energy, the SET is a quantum mechanical system. While a single electron is bound to the law of energy conservation, it is possible for two or more electrons to tunnel simul-

taneously. The tunneling electrons then do not need to conserve energy individually but only as a whole, thereby giving rise to new contributions to the charge current. These are called cotunneling contributions and are of higher order in the system-lead interaction than the sequential tunneling contributions we have discussed so far. In this thesis, we will concentrate on sequential tunneling only. It is however important to be aware of the existance of cotunneling effects. They become important for strong system-lead interactions or when all other transitions are forbidden. In order to stay in the sequential tunneling regime, it is therefore necessary to enforce that the system-lead interaction is weak compared to all other energyscales in the problem, including the temperature of the system. In the free transport regime, sequential tunneling contributions then dominate the system dynamics since the cotunneling contributions are of quadratic or higher order in the system-lead interaction and therefore smaller than the first order contributions. In the Coulomb blockade regime, where the sequential tunneling contributions can vanish, however, cotunneling can become important. Here, finite sequential tunneling contributions can be generated via thermal flucuations. If the thermal energy is larger than the system-lead coupling strength, these contributions dominate the cotunneling effects which can then safely be ignored.

2.2. Vibrational Sidebands and Spin-Polarized Currents

We have illustrated the basic mechanism of single-electron transport and some of its qualitative effects using the example of the single-electron transistor. The model which we used for the single-electron transistor does not include spin-polarized transport or interactions between vibrational and electronic degrees of freedom. The main topic of this thesis, however, is to investigate nanotransport in systems including both magnetic and vibronic degrees of freedom simultaneously. A review of the literature analyzing the effects of each of these two components on quantum transport will help to understand the results presented throughout this thesis. In the following we therefore review selected literature on each of these topics.

2.2.1. Franck-Condon Blockade

Previously we have argued how single-electron transfer allows us to make a connection between the energy spectrum of a quantum dot and its current-voltage characteristics. The current flow through a nanoelectric device such as the SET can be blocked as a result of Coulomb interactions. By varying the bias and gate voltages, the Coulomb

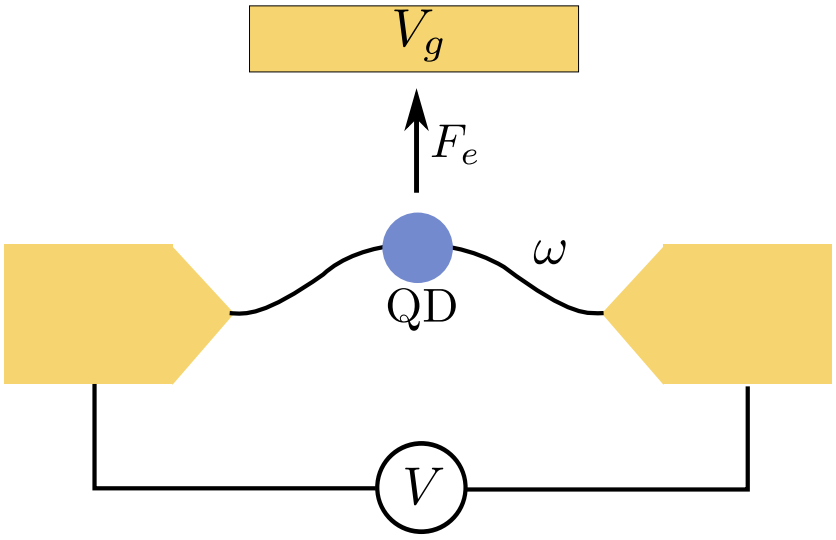

Figure 4: Schematic of a quantum dot (QD) embedded on a nanobeam with frequency ω. Bias (V) and gate (V_g) voltage couple electronic charge flow through the quantum dot to the vibrations of the nanobeam. The resulting shift of the oscillator equilibrium position can induce a phonon blockade of the current.

blockade can be lifted. The emerging structure is known as Coulomb diamonds and yields information about the energetic position of the charge states of the SET. A blockade of the charge current however can also be induced by interactions between electronic and mechanical degrees of freedom. An example for a system where such an effect occurs is a nanomechanical resonator coupled to a single-electron transistor as schematically shown in Figure 4. The electrostatic potential induced by the gate electrode of the SET induces a force F_e on the charges. If the single-electron transistor is embedded on the nanoresonator, the induced force will lead to a shift of the equilibrium position of the resonator. In the same way, any vibration of the nanoresonator will lead to a shift of the energies of the SET. If this shift is sufficiently strong, transport through the SET is prohibited and a phonon blockade occurs. For quantum oscillators in the regime of a strong coupling between electronic and vibrational degrees of freedom such effects have been predicted [7, 8] and measured in molecular devices [16, 23, 24]. A strong electron-phonon coupling leads to a suppression of the current known as the Franck-Condon blockade [9, 13, 15]. Furthermore, the eigenfrequency of the oscillator can be read from the current-voltage characteristics of such devices. Each charge state of the SET is coupled to the vibrational states of the nanoresonator. These vibrational

sidebands create additional transport channels. A signature of this effect can be found as equidistant steps in the current, separated by the eigenfrequency of the vibrational mode, referred to as Franck-Condon steps. The same model can be used to describe transport through molecules where the occupation of different orbitals affects the vibrational modes of the molecule and vice versa. The phonon blockade vanishes for very weak electron-phonon interactions or in the limit of high temperatures. In the regime of strong coupling between leads and nanodevice or in the strong electron-phonon coupling regime, Franck-Condon effects become more pronounced and the phonon blockade dominates the transport properties of the nanodevice or molecule. Further enhancement of a phonon-induced current blockade is possible by driving the nanoresonator into the Euler buckling instability [19, 21]. Here, the frequency of the fundamental bending mode of the oscillator softens and a strong enhancement of the current noise can be found [20].

2.2.2. Spin-Polarized Currents

So far we have considered electrons as spinless fermionic particles. In the following two chapters, we aim to discuss spin-polarized transport through nanodevices. A spin-polarized current can be generated by using ferromagnetic leads. A ferromagnetic solid is characterized by a different density of states for different spin carriers. One typically distinguishes between electrons carrying a spin pointing upwards on the quantization axis and electrons with a spin pointing downwards on the quantization axis. In a non-magnetic solid, the density of states at the Fermi level for both types is equal. In a ferromagnetic solid, the density of states for one spin direction is higher than for the other. The spin directions can then be referred to as majority and minority spins. The relative difference in the density of states between majority and minority spin carriers is called the polarization.

Let us next replace the lead electrodes of the SET by ferromagnetic leads with a high degree of polarization. Let us further assume that the source and the drain lead are fully polarized in opposite directions. If now an electron tunnels from the source lead onto the dot, its spin will point in the direction of the majority spin of the source electrode. The drain electrode is polarized into the opposite direction. For a fully polarized material this means that the density of states for minority spin carriers is equal to zero. The electron on the dot therefore has no possibility to tunnel into the drain since there are no states available. The polarization of the leads thus creates a spin-blockade. Spin blockades and related phenomena have been observed in both single and double quantum dot setups [61, 62]. Combining ferromagnetic leads with an external magnetic field or

a local magnetization on the quantum dot can lead to precession of the electronic spin [27, 28]. These effects are induced by noncollinear orientations of the lead polarizations and/or an external magnetic field. It can be shown that the linear conductance of a spin valve depends heavily on the relative angle between the leads magnetization directions. Different orientations of the lead polarizations lead to spin accumulation on a quantum dot or spin valve [32, 33, 63]. Signatures of a spin accumulation can be found in both the current as well as the current noise. The interactions between the nanodevice and the ferromagnetic leads can be expressed as an effective magnetic field acting on the magnetic degrees of freedom of electrons or local impurity spins [30, 31] on the device. Here, the charging energy of the device plays an important role as found in analytic calculations of the effective field. This leads to the possibility to create nanodevices and spin-valves with negative differential conductance [64].

2.3. Quantum Master Equation

In order to make both qualitative and quantitative statements about systems away from thermal equilibrium such as the ones in the previously reviewed literature, it is necessary to formulate a theoretical framework for analytical or numerical calculations. The framework used throughout this thesis is provided by the quantum master equation approach. To provide a clear and transparent view over our results, we therefore have to explain the basic concept of the master equation. In the following, we derive a quantum master equation for the reduced density matrix of an open quantum system.

2.3.1. Derivation

The first step of our derivation is to identify the system which we want to investigate. A common approach to describe open quantum systems is the system-bath model [65]. Let us assume that we have a nanodevice coupled to two electronic charge reservoirs by tunnel junctions. The Hamiltonian for the system and the environment can then be written as

$$H = H_{sys} + H_{lead} + H_{int}, \tag{3}$$

where H_{sys} represents the nanodevice, H_{lead} the electronic leads and H_{int} the interaction between the system and the leads. The Hamiltonian of the system $H_{sys} = H_{sys}(A, A^\dagger)$ is a function of the electron annihilation and creation operators A, $A^\dagger$, respectively. At this point, it is not necessary to give a more specific definition of the system. As we

have already seen in our analysis of the SET, the energy spectrum of the nanodevice is of importance. We define the eigenenergies ϵ_χ of the system by $H_{sys}|\chi\rangle = \epsilon_\chi|\chi\rangle$, where $|\chi\rangle$ are the eigenstates of the nanodevice. The leads are modelled as non-interacting Fermi gases in the form of

$$H_{lead} = \sum_{k,\alpha} \epsilon_{k,\alpha} B^\dagger_{k,\alpha} B_{k,\alpha}, \tag{4}$$

where $B_{k,\alpha}$ and $B^\dagger_{k,\alpha}$ are the annihilation and creation operators for electrons in lead α with wavevector k, and $\epsilon_{k,\alpha}$ defines the chemical potential. The Hilbert space of the system and the environment is then spanned by the product of the corresponding eigenstates $|\psi\rangle = |\varphi\rangle|\chi\rangle$. Interactions between the system and the environment consist of the exchange of electrons. This is described by the interaction Hamiltonian

$$H_{int} = \sum_{k,\alpha} \left(t_{k,\alpha} A^\dagger B_{k,\alpha} + \text{h.c.} \right), \tag{5}$$

where $t_{k,\alpha}$ is the tunneling amplitude. In contrast to the previous section we have now chosen an explicit form for the interaction between system and environment. The interaction Hamiltonian (5) describes the tunneling of an electron between system and lead. A full description of the system and the environment is, in most cases, impossible due to the size of the environment. It is, however, possible to describe the dynamics of only the system by integrating out the environment. An approach based on this technique is the quantum master equation [66]. The master equation describes the evolution of the reduced density matrix via transition rates between the system and the environment. The reduced density matrix is obtained by tracing over the degrees of freedom of the environment, $\rho(t) = \text{Tr}_\text{l}\left[\text{W(t)}\right]$, where $\text{Tr}_\text{l}\left[...\right]$ denotes the trace over the leads. The master equation can be derived starting with the Liouville-von-Neumann equation for the full density operator $W(t)$ in the interaction picture

$$\dot{W}^I(t) = -\frac{i}{\hbar}\left[H^I_{int}(t), W^I(t)\right], \tag{6}$$

where the superscript I denotes operators in the interaction picture defined as $O^I(t) = e^{iH_0(t-t_0)/\hbar} O(t) e^{-iH_0(t-t_0)/\hbar}$ with $H_0 = H - H_{int}$. The formal solution of this equation

can be found by integration

$$W^I(t) = W_0^I - \frac{i}{\hbar}\int_{t_0}^{t} dt' \left[H_{int}^I(t'), W^I(t')\right]. \tag{7}$$

Now, it is possible to reinsert the solution into Eq.(6) and iterate the equation. One obtains

$$\dot{W}^I(t) = -\frac{i}{\hbar}\left[H_{int}^I(t), W_0^I\right] - \frac{1}{\hbar^2}\int_{t_0}^{t} dt' \left[H_{int}^I(t), \left[H_{int}^I(t'), W^I(t')\right]\right]. \tag{8}$$

Notice that this equation is formally exact since all orders of the system-lead interaction are included either explicitly in form of the interaction Hamiltonian or implicitly in the density matrix. Since the goal is the derivation of an equation of motion for the reduced density matrix, the next step is to trace over the lead degrees of freedom. A general assumption at this point is to consider each lead itself to be at thermal equilibrium at all times. In order for this assumption to be valid two conditions need to be fulfilled: First, the equilibration time of the leads needs to be fast compared to the time between two tunneling processes. Second, the leads need to be very large compared to the system. The addition or removal of a finite number of electrons from the leads must not change their state. Alternatively, we can place the leads in thermal contact with an infinitely large superbath, which enforces a thermal distribution. Since we are discussing the transfer of single electrons between a nanosystem and its environment typically given by solids of macroscopic dimension, these assumption are valid. The density operator of the leads is then given by the equilibrium distribution $\rho_{lead}^{eq} = \frac{1}{Z_l} e^{-\beta H_{lead}}$ with the partition function $Z_l = \mathrm{Tr_l}\left[e^{-\beta H_{lead}}\right]$ and $\beta = (k_\mathrm{B}T)^{-1}$. In order to proceed, we now assume that the initial density operator $W_0 = W(t=0)$ can be factorized into the density operator of the subsystem $\rho(t) = \mathrm{Tr_l}[W(t)]$ and the equilibrium distribution of the leads, $W_0 = \rho_{lead}^{eq} \otimes \rho(t=0)$. The interaction Hamiltonian H_{int} is non-diagonal in the eigenbasis of the leads. Consequently, the first term on the right-hand side of Eq. (8) vanishes if we trace over the lead degrees of freedom, leading to

$$\dot{\rho}(t) = -\frac{i}{\hbar}\left[H_0, \rho(t)\right] - \frac{1}{\hbar^2}\mathrm{Tr}_l\left\{\int_{t_0}^{t} dt' \left[H_{int}^I(t), \left[H_{int}^I(t'), W^I(t')\right]\right]\right\}. \tag{9}$$

The first term on the right-hand side appears when transforming the reduced density matrix on the left-hand side back into the Schrödinger picture. Equation (9) is the quantum master equation for the reduced density matrix. The first term describes reversible

motion and yields coherent oscillations between quantum states of the subsystem. It contains no information about the bath or dissipative effects. The second term contains all interactions between the bath and the system. It gives rise to irreversible dynamics and effects like relaxation, decoherence or dephasing. Approximate solutions to the master equation can be found in various ways. A review of different types of master equations and the corresponding solution methods is given in Ref.[67].

2.3.2. Redfield Master Equation

The approach pursued in this thesis is the numerical solution of the Redfield master equation by using diagrammatic perturbation theory. The Redfield equation follows from the master equation (9) by making two approximations.

The first approximation is to assume Markovian dynamics. On the right-hand side of Eq. (9), we see that the evolution of the density matrix depends on the interaction Hamiltonian and the density matrix at all previous times. Depending on the form of the environment surrounding the system of interest, it is possible that a calculation of the systems dynamics requires to take into account the previous dynamics up to a certain memory time τ. Such effects can appear for example in complex biomolecules [68]. Another example is the nonequilibrium quantum transport in the Anderson model in the regime of large Coulomb repulsion U [69]. The dynamics of such a system is then called non-Markovian. For Markovian systems, the memory time is assumed to be much shorter than any system or bath time scale ω_c^{-1}, i.e. $\tau\omega_c << 1$. Let us rewrite Eq. (9) in order to perform a Markovian approximation in the form

$$\dot{\rho}(t) = -\frac{i}{\hbar}\left[H_0, \rho(t)\right] - \frac{1}{\hbar^2}\mathrm{Tr}_l\left\{\int_{t_0}^{t} dt' M(t,t')W(t')\right\}. \tag{10}$$

Here we have renamed the double commutator by the integral kernel $M(t,t')$. Now we want to assume that the system exhibits Markovian behaviour. The integral kernel $M(t,t')$ should then be peaked around the time t and be given by a δ-function, i.e.,

$$M(t,t') \approx \bar{M}(t)\delta(t-t'), \tag{11}$$

with $\bar{M}(t) = \int_{t_0}^{t} dt' M(t,t')$. We can now perform the original time integration and replace the kernel once again by the double commutator leading to

$$\dot{\rho}(t) = -\frac{i}{\hbar}\left[H_0, \rho(t)\right] - \frac{1}{\hbar^2}\mathrm{Tr}_l\left\{\int_{t_0}^{t} dt' \left[H_{int}^I(t), \left[H_{int}^I(t'), W^I(t)\right]\right]\right\}. \tag{12}$$

The second approximation we want to perform is a weak-coupling approximation. If the contact between the system and the environment is sufficiently weak, it is reasonable to assume that only the lowest order of the interaction is important for the system's dynamics. We will therefore assume that the density matrix $W^I(t)$ does not depend on the system-lead interaction. Consequently, since we have iterated the equation only once, this assumption yields the master equation to lowest order in the system-lead interaction and is only valid when the interaction strength $t_{k,\alpha}$ is weak compared to other energy scales in the problem. The evolution of the reduced density matrix can now be determined by expanding the double commutator and performing the integration. Carrying out the trace over the bath degrees of freedom and using the factorization of the density matrix finally yields the Redfield equation for the components of the reduced density matrix in the form

$$\dot{\rho}_{ab}(t) = -\frac{i}{\hbar}(\epsilon_a - \epsilon_b)\rho_{ab}(t) - \sum_{cd} R_{abcd}\rho_{cd}(t). \tag{13}$$

Here R_{abcd}, denotes the Redfield tensor containing the rates obtained by evaluating the second term on the right hand side of Eq.(12). The indices a, b, c, d refer to energy eigenstates of the system Hamiltonian. The Redfield equation has many applications in physics and chemistry. It is a well-established method to describe processes like nuclear magnetic resonance [70], optical methods [71] or quantum transport in nanodevices [67]. In nuclear magnetic resonance, the Redfield equation can be used to describe the relaxation dynamics of the spin system in a paramagnetic environment. In a similar way the dynamics of optically excited systems can be determined by a set of equation derived from the Redfield approach. These equation are known as the optical Bloch equations [72]. Transfer of excitation energy in biomolecules can also be investigated by using of the Redfield equation [73].

2.3.3. Diagrammatic Perturbation Theory

One particular way of obtaining the Redfield rates is the diagrammatic perturbation theory [58]. The rates which form the Redfield tensor can be represented by Feynman diagrams [66, 74] up to first order in the tunneling. In order to understand this method we first have to give a brief introduction into diagrammatic methods for equilibrium dynamics and then introduce the corresponding method for non-equilibrium physics [75].

Feynman diagrams have been developed by R. Feynman in 1948 as a tool to simplify the calculation of Green's functions in quantum field theory. A Green's function $G(x,t;x',t')$ describes the time evolution of a system from time t' at x' to a state x at time t. Let us assume a scattering problem: We have a system or particle which interacts with a different particle at time $t=0$ given by the interaction $V(t)$. Initially, at $t\to-\infty$, both particles are separated and do not interact. The same is valid for very long times after the scattering process, $t\to\infty$. We can then define the time-ordered Green's function as

$$G(x,t;x',t') = -\frac{i}{\hbar}\frac{\langle\Psi_0|T\left\{\psi_H(x,t)\psi_H^\dagger(x',t')\right\}|\Psi_0\rangle}{\langle\Psi_0|\Psi_0\rangle}, \tag{14}$$

where T denotes the time-ordering operator, $|\Psi_0\rangle$ the ground state of the system and $\psi_H(x,t)$ the field operator in the Heisenberg picture. The definition of the Green's function contains the exact ground state of the system which is one of the quantities that one usually wants to calculate using the Green's function. However, we can express the ground state of the interacting system in terms of the ground state of the non-interacting system $|\Phi_0\rangle$ and the scattering matrix $S(t,t')$. According to the Gell-Mann and Low theorem, the ground state is given by

$$|\Psi_0\rangle = S(0,-\infty)|\Phi_0\rangle. \tag{15}$$

We then find for the time-ordered Green's function

$$G(x,t;x',t') = -\frac{i}{\hbar}\frac{\langle\Phi_0|T\left\{S(\infty,-\infty)\psi(x,t)\psi^\dagger(x',t')\right\}|\Phi_0\rangle}{\langle\Phi_0|S(\infty,-\infty)|\Phi_0\rangle}. \tag{16}$$

This new expression allows us to calculate the Green's function by performing a perturbative expansion in the interaction $V(t)$. We expand the scattering matrix according to

$$S(\infty,-\infty) = \sum_{n=0}^{\infty}\frac{(-i)^{n+1}}{n!}\int_{-\infty}^{\infty}dt_1...dt_nT\left\{V(t_1)...V(t_n)\right\}. \tag{17}$$

Each interaction term contains several field operators $\psi(t)$. In order to calculate the time evolution of the system, we therefore need to be able to determine expectation

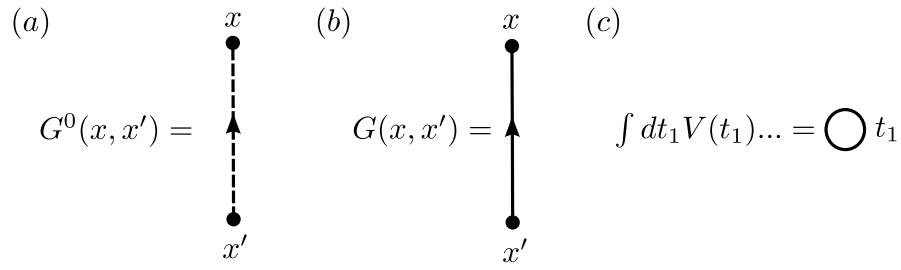

Figure 5: Graphical representation of the free Green's function (a), the full Green's function (b) interaction (c).

values of the type

$$\langle \Phi_0 | T \left\{ \psi(t)\psi^\dagger(t')\psi^\dagger(t_1)\psi^\dagger(t_2)\psi(t_2)\psi(t_1) \right\} | \Phi_0 \rangle, \tag{18}$$

and similar expressions. The Wick theorem [76] states that these expressions are given by the sum of all pairwise contractions. Finding all contractions can become a tedious and complicated task depending on the complexity of the system. The Feynman diagrams, however, are pictorial representations of exactly these expectation values. Each diagram denotes a very specific contribution of our expansion. Figure 5 shows the most fundamental components for diagrams needed to describe the scattering problem. Using only these tools it is possible to write down a graphical representation of the Dyson equation [77] as shown in Figure 6.

The discussion up to this point refers to the use of the diagrammatic representation in equilibrium systems. Our brief motivation, however, already illustrates the fundamental difference and difficulty we have to face when we want to apply the method to non-equilibrium physics. In our derivation of a pertubation series for the Green's function, the scattering matrix plays a central role. In equilibrium, we were able to rewrite the exact ground state of the system due to the fact that it relaxes into its initial ground state for infinitely large times. In non-equilibrium, however, this is not possible. There is no guarantee that the system returns to its initial state at any time. A solution of this problem can be found in form of the Keldysh technique. Instead of defining the time-ordered Green's function, we define a contour ordered Green's function. Instead of going from an initial time t_0 to a final time t_f as shown in Figure 7 (a), the Keldysh contour goes back to the initial time t_0 as shown in Figure 7 (b). Setting the initial time to minus infinity ($t_0 \to -\infty$) now allows us to use the perturbation series of the

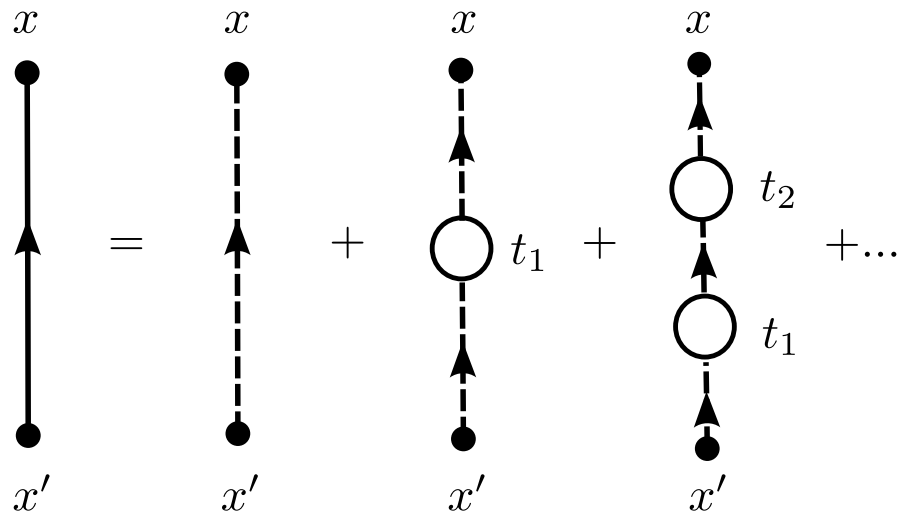

Figure 6: Perturbation series for the full Green's function using the diagrammatic representation.

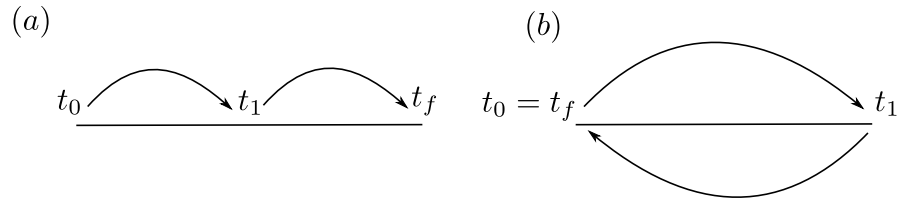

Figure 7: Time-ordering for (a) equilibrium Green's functions and (b) non-equilibrium Green's functions according to the Keldysh contour.

scattering matrix once again. The expression for the non-equilibrium Green's function is then structurally equivalent to the equilibrium example.

We next apply the diagrammatic techniques to the Redfield equation. The goal is to express the rates included in the Redfield tensor by diagrams on the Keldysh contour. In Figure 8 (a), we show the building elements of the diagrams we use to represent the Redfield tensor. Figure 8 (b) shows one of the contributions of the integral kernel $M(t, t')$ represented as a diagram. The solid lines represent the free propagation of the system on the Keldysh contour in the respective state. The upper line in Figure 8 (b) stands for propagation forward in time whereas the lower line is the backward propagator as we illustrated in Figure 7 (b). The propagation direction is indicated by arrows. Each free propagator is labelled with the state occupied by the system. The filled dots indicate a

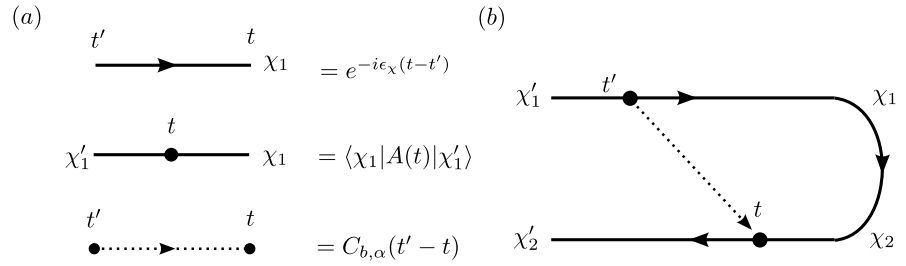

Figure 8: (a) Basic elements for the real-time diagrams on the Keldysh contour. Solid lines with an arrow indicate free propagation of the system. A vertex, symbolizing interactions between the system and the bath, is indicated by a solid circle on a propagator line. The tunneling of electrons between system and bath is represented by dashed, directed tunneling lines between each pair of vertices. The corresponding values for each of this contributions according to the diagrammatic rules are given in the Figure. (b) Diagrammatic representation of a first-order tunneling process.

vertex, i.e., an interaction between the bath and the system according to H_{int}. A pair of vertices of connected by a dashed, directed line, the tunneling line. A dashed line going out of the vertex symbolizes an electron tunneling from the system to the bath and an ingoing line symbolizes the opposite process. The number of electrons associated with the states of each propagator and tunneling line directed towards the vertex must be equal to the corresponding number of electrons for all propagators and tunneling lines directed away from the vertex.

The diagrammatic method has the advantage that the perturbation in the tunnel coupling can be handled in a very intuitive way. In order to take into account only the lowest order of system-bath interactions as it has been done in the derivation of the Redfield equation, one only needs to draw all diagrams with a single tunneling line. Higher order interactions leading to cotunneling contributions contain more than one tunneling line. To calculate the evolution of the reduced density matrix, the Redfield tensor can be replaced by a sum over all first-order diagrams. There is a total of eight diagrams with one tunneling line which are shown in Figure 8 (b). To determine the contribution of each diagram, the following rules can be used [30, 31]:

- Draw all topologically different diagrams with directed tunneling lines between pairs of vertices. Assign states, energies and bath indices to all vertices and tunneling lines.

- Each propagator on the Keldysh contour with state χ from time t' to t implies a factor $e^{-i\epsilon_\chi(t-t')}$.

- Each vertex between two states χ and χ' containing a system operator A implies a factor $\langle\chi'|A|\chi\rangle$, where χ is the incoming and χ' the outgoing state on the Keldysh contour.

- A directed tunneling for reservoir α from t' to t implies a factor $C_{k,\alpha}(t'-t)$ for tunneling lines forward and $C^\dagger_{k,\alpha}(t-t')$ for tunneling lines backward on the Keldysh contour. Here, $C_{k,\alpha}(t-t') = \langle B^\dagger_{k,\alpha}(t)B_{k,\alpha}(t')\rangle$ denotes the bath correlation function at wavevector k.

- Each diagram carries a prefactor $-(-1)^m$ where m is the number of vertices on the lower contour. Additional minus signs can appear due to ordering of the electronic operators in the case of multi-electron states.

- Sum over all combinations of ingoing and outgoing states. Each diagram has to be integrated over the time $\int_{t_0}^{t} dt'$.

Let us compare the diagrammatic rules with the results obtained by expanding the double commutator in Eq. (12) in order to understand their origin. The double commutator reads

$$\begin{aligned}\left[H^I_{int}(t),\left[H^I_{int}(t'),W^I(t)\right]\right] &= H^I_{int}(t)H^I_{int}(t')W^I(t) - H^I_{int}(t)W^I(t)H^I_{int}(t') \\ &\quad -H^I_{int}(t')W^I(t)H^I_{int}(t) + W^I(t)H^I_{int}(t')H^I_{int}(t). \qquad (19)\end{aligned}$$

By inserting the definition of the interaction Hamiltonian (5), the third term yields

$$\begin{aligned}&\langle\varphi|H^I_{int}(t')W^I(t)H^I_{int}(t)|\varphi\rangle = \\ &|t_{k,\alpha}|^2\textstyle\sum_k\langle\varphi|A^\dagger(t')B_{k,\alpha}(t')W(t)B^\dagger_{k,\alpha}(t)A(t) + B^\dagger_{k,\alpha}(t')A(t')W(t)A^\dagger(t)B_{k,\alpha}(t)|\varphi\rangle, \qquad (20)\end{aligned}$$

where we have now omitted the superscript for the interaction picture. Due to the trace over the bath all pairings of two lead electron annihilation or two lead electron creation operators vanish. Using the factorization of the density matrix leads to

$$\begin{aligned}&\langle\varphi|H_{int}(t')W(t)H_{int}(t)|\varphi\rangle = \\ &|t_{k,\alpha}|^2\textstyle\sum_k\left[A^\dagger(t')A(t)\rho(t)C^\dagger_{k,\alpha}(t'-t) + A(t')A^\dagger(t)\rho(t)C_{k,\alpha}(t'-t)\right]. \qquad (21)\end{aligned}$$

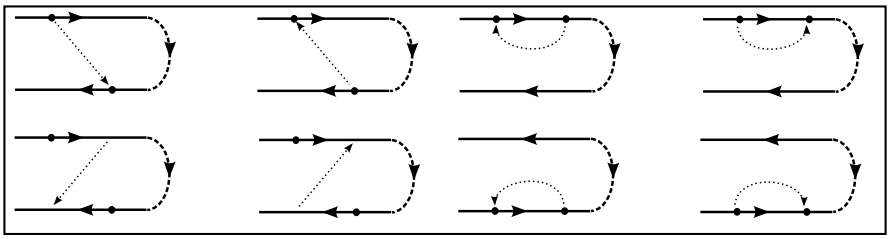

Figure 9: Schematic of all eight different diagrams contribution to the first order transitions in the master equation.

The second term on the right-hand side describes the diagram depicted in Figure 8 (b). All other diagrams can be found in the same way via the expansion of the commutator. Drawing all topological diagrams and applying the diagrammatic rules is therefore equivalent to a direct calculation of the Redfield tensor. A schematic of all different first-order diagrams appearing in the master equation of our system is shown in Figure 9. Since the Feynman diagrams are an exact representation of the perturbation theory in the system-lead interaction, it would in principle be possible to calculate the next order in the tunnel coupling by drawing all diagrams with two tunneling lines. Due to the large amount of combinations, a diagrammatic approach yields a huge advantage over a direct calculation of the resulting commutators. In this thesis, however, we will restrict ourselves to the first order contributions.

2.3.4. Numerical Solution

The Redfield equation (13) gives rise to a set of coupled differential equations for the elements of the reduced density matrix of our nanodevice. For small systems an analytical solution is possible [28, 30, 57]. Depending on the dimension of the Hilbert space of the system, however, a numerical calculation is preferable. In the following we therefore discuss briefly how to find a numerical solution for the full Redfield equation. The stationary solution of the master equation is given by

$$0 = \widetilde{R}\boldsymbol{\rho}_{stat}(t), \tag{22}$$

where we have absorbed the zeroth order term describing the coherent dynamics of the quantum system into the modified Redfield tensor $\widetilde{R}$. To simplify numerical calculations we rearrange the density operator into a vector $\boldsymbol{\rho}_{stat}(t)$ such that the Redfield

tensor becomes a matrix. The calculation of the stationary solution then reduces to an eigenvalue problem for the matrix $\widetilde{R}$. Finding the eigenvalues of a matrix is a task which can be fulfilled by common numerical methods.

To determine the time evolution of the reduced density operator, we first find the formal solution of the Redfield equation

$$\boldsymbol{\rho}(t) = e^{\widetilde{R}(t-t_0)}\boldsymbol{\rho}(t=0). \tag{23}$$

The formal solution can be expanded in terms of the left and right eigenvectors of $\widetilde{R}$, such that

$$\rho(t) = \sum_m \boldsymbol{v}_{mL}^\dagger \boldsymbol{\rho}(t_0) e^{\Gamma_m(t-t_0)} \boldsymbol{v}_{Rm}, \tag{24}$$

where $\boldsymbol{v}_{L/Rm}$ denote the the left/right eigenvectors and Γ_m the eigenvalues of the modified Redfield tensor. Knowledge of the time evolution of the reduced density matrix then allows us to calculate expectation values of any operators, such as, for example, average spin projections, the number of electrons on a quantum dot or the occupation of vibrational states. Using diagrammatic methods, it is also possible to determine the charge current flowing through the device. The charge current can be defined as the time derivative of the number of electrons on the nanodevice,

$$I = e\langle\frac{\partial n}{\partial t}\rangle. \tag{25}$$

The change in the electronic occupation number n can be determined by summing over all diagrams in which the number of electrons on the device changes between t' and t, i.e. the four diagrams on the left side of Figure 9. The average charge current is then given by the expectation value of these contributions.

By this, we have now a method at hand which allows us to calculate the expectation value of any system operator both in the steady state as well at any other given time. The method requires knowledge of the bath correlator, the system-bath interaction and the eigenenergies of the system only. We are, however, limited to a description of systems which interact weakly with their environment and are dominated by Markovian dynamics.

3. Cooling Nanodevices via spin-polarized Currents

The continuous effort of miniaturizing electronic devices leads to several new challenges. One of these challenges is the requirement to develop efficient cooling mechanisms for micro- and nanoelectronics. To date most electronic devices utilize passive cooling techniques. Thermal contact with the supporting structure provides the possibility to use the environment as a passive heat sink. Active or dynamical nano-cooling has received little attention, although passive thermal transport is inefficient at the nanoscale. Furthermore, most of the recently developed electronic and magnetic nanodevices operate at low temperatures only. The importance of a dynamical cooling mechanism on the nanoscale can therefore not be underestimated. Dynamical nanorefrigerators would also open the possibility for new experiments and devices. Most dynamical cooling methods require spacious equipment and mechanical movement (of pumping equipment, for example) thus making them impractical for an application on nanodevices. Manipulating the heat on the nanoscale would then not only drastically decrease the size of the cooling equipment, but also yield the possibility to create arrays of cooled nanodevices.

The most accessible part of many nanodevices are the electronic degrees of freedom. By applying external bias voltages, it is often not only possible to control charge currents, but also magnetic or mechanical properties. There are proposals for nanorefrigerators in which heat is carried by an electronic charge current [36]. In this work, we propose a cooling mechanism which utilizes the electronic spin rather than the charge in order to achieve a net cooling effect. The cooling mechanism is a nanoscale adaption of the magnetocaloric demagnetization cooling [40] which is an example of a successful cooling method on the macroscale using magnetic degrees of freedom.

The chapter is structured as follows. In the first section, we motivate the cooling concept by explaining the magnetocaloric demagnetization cooling and discussing an adaption to the nanoscale. A proof of principle model for the nanocooling scheme is introduced in the second section. The model is compared with recent experiments [41–43, 78]. We analyze the energy spectrum and give a brief synopsis of the numerical method in the third section. The fourth and fifth section are dedicated to a description of the principle mechanism of the cooling setup and its initial preparation, respectively. Section 3.6 displays the numerical results. We compare different lead setups with respect to their cooling efficiency and identify the most favourable cooling setup. As the main result of this chapter, we show a decrease of the effective temperature to about 50% of its initial value. A summary and conclusion of the results is provided in the final

section.

3.1. Cooling Scheme

Using the spin degree of freedom to cool a macroscopic sample of matter is a mechanism which first has been suggested in 1927 by Peter Debye and William F. Giauque [79]. The mechanism is known as demagnetization cooling and lead to the development of the first magnetic refrigerators with the ability to cool samples to temperatures below 0.3 K. These magnetic refrigerators utilize changing magnetic fields in order to invoke a change in temperature. The core principle of the demagnetization cooling is the transformation of thermal energy into magnetic energy in an isolated sample as part of a reorientation process of the magnetic moments. In order to develop a magnetic refrigerator a thermodynamic cycle can be built around this principle. An example of such a cooling cycle (see Figure 10) consists of four steps:

(I) Adiabatic magnetization: A magnetic substance is placed in an isolated environment without any thermal contact. An increasing external magnetic field H causes the magnetic moments of the substance to align. Since the substance is isolated, both the entropy and the energy have to be conserved. This leads to an increase in the temperature ($T \to T + \Delta T$) to compensate for the decrease in the magnetic entropy.

(II) Isomagnetic enthalpic transfer: In order to remove the added heat it is necessary to bring the substance in thermal contact with a coolant. The magnetic field is held constant during this phase in order to keep the magnetic moments from reabsorbing the heat. Once the magnetic solid is cooled down to its initial temperature ($T + \Delta T \to T$) the coolant can be removed thus once again isolating the magnetic substance.

(III) Adiabatic demagnetization: In the third step, the magnetic field is decreased causing the magnetic moments to overcome the field. Since both energy and entropy are once again conserved the relaxation of the magnetic moments leads to a decrease of the temperature ($T \to T - \Delta T$) in the substance.

(IV) Isomagnetic entropic transfer: Now, the magnetic field is held constant and the substance is brought into thermal contact with the sample which is to be cooled. The resulting heat exchange cools the sample, while bringing the solid back to its original temperature ($T - \Delta T \to T$). Once a thermal equilibrium is reached the cycle can be restarted.

While being successfully applied on the macroscale, a conceptual difficulty of these magnetic refrigeration cycles is the opening and closing of heat links. In a macroscopic setup, the transfer of the excess heat to a coolant (step (II)) requires either to pump

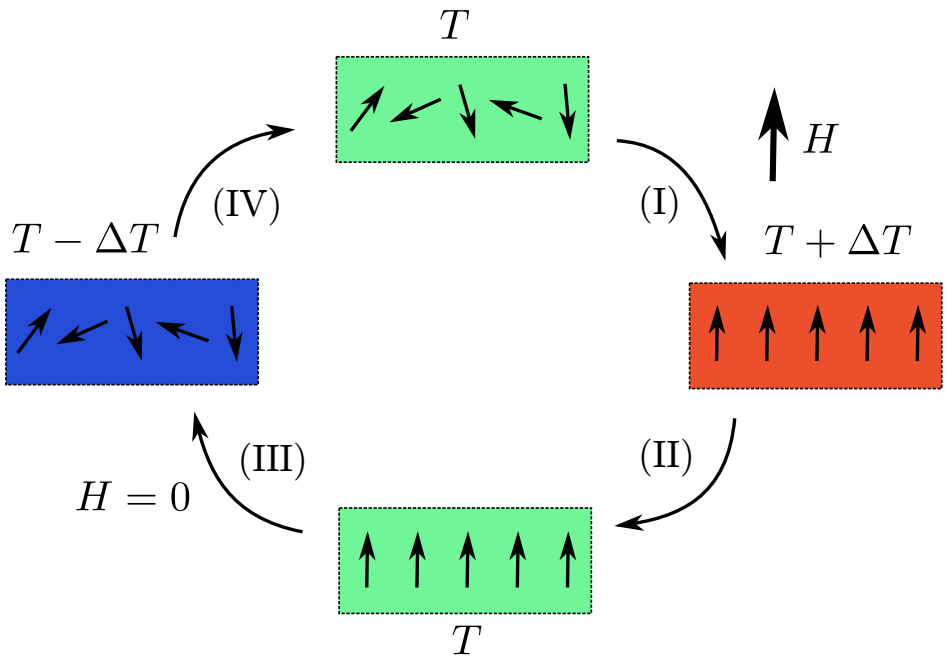

Figure 10: Illustration of the demagnetization cooling cycle. The cycle consists of four steps: In step (I) an external magnetic field H polarizes the sample and leads to an increase of the thermal energy. Step (II) is the extraction of the excess heat ΔT via thermal contact with a coolant. Isolating the sample and turning off the external field in step (III) lead to a relaxation of the magnetic moments at the cost of thermal energy. The last step (IV) closes the cycle by putting the sample in thermal contact with the material which we want to cool.

the coolant or mechanical movement of the magnetic substance. In the same way, thermal contact between substance and sample (step (IV)) has to be established. These technical constraints of the cooling cycle complicate an adaption to the nanoscale. Here, mechanical movement of the setup or large cooling equipment proves impractical for most applications to nanodevices. An example would be the development of microchips to the nanoscale where they are to be used in large numbers as part of electronic hardware [80]. Movement of individual microchips or even arrays of microchips as part of their cooling concept will interfere with their application. Additionally, the use of changing external fields for magnetization hinders an application of such a cooling scheme for magnetic memory devices.

Nonetheless, the nanocooling scheme we propose here is also based on the exchange of energy between magnetic and phononic degrees of freedom. The core of our concept is the use of spin-polarized currents in order to generate a magnetization. Contrary to the macroscale cooling cycle which relies on equilibrium thermodynamics, we use transport properties of nanodevices to develop a non-equilibrium cooling scheme. The main advantage of a magnetization via spin-polarized currents is the ability to control the contact between sample and environment all-electronically by using bias voltages. This environment is represented by ferromagnetic leads or spin-polarized electron reservoirs. Applying a bias voltage to the leads generates the flow of a spin-polarized current through the nanodevice. The polarized spins can interact with the local magnetization of the device via exchange coupling thus replacing the function of the external field H of the macroscopic setup. It is therefore possible to generate and control the magnetization of the sample directly by using its charge transport properties. Additionally, the contact to the environment allows the transfer of entropy and energy between system and environment, thereby reducing the heat generated by the magnetization process (step (I)). The polarization of the local magnetization of the nanodevice by the current forces the device into the spin ground state, thereby lowering its energy. A magnetomechanical coupling between the local magnetization and the vibronic degrees of freedom then enables the spins to relax again by reducing the vibrational energy and thus cooling the device. An externally applied electric current, however, gives rise to Ohmic heating effects. The spin-polarized current thus induces two effects: A reduction of the magnetic energy of the device, and, a heating due to Ohmic losses. An effective cooling protocol can only be established if the cooling effect due to magnetization exceeds the heating generated by Ohmic losses. This is possible as will be shown in the following sections.

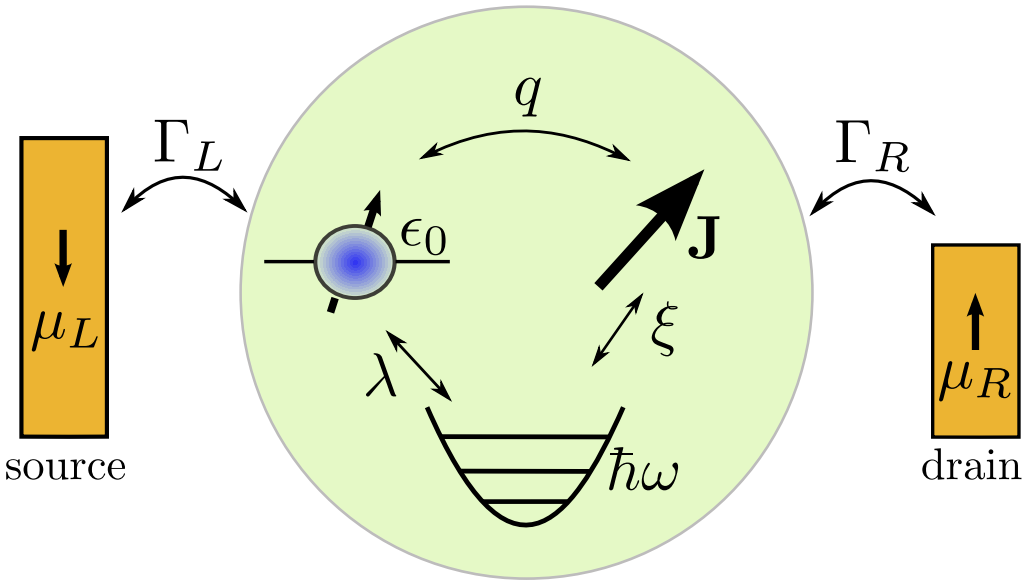

Figure 11: Schematic consisting of ferromagnetic leads, a quantum dot with a localized magnetic moment and a single vibrational mode.

3.2. Model

In order to determine the nonequilibrium spin and phonon dynamics of such a nanorefrigerator, we employ a minimal model as a proof-of-principle. Its minimal ingredients consist of a magnetic quantum dot with a single electronic level, a local magnetic moment $\boldsymbol{J}$ and a single vibrational mode as sketched in Fig. 11. Ferromagnetic leads are weakly coupled to the quantum dot via tunneling thus allowing for spin and charge transport. We note that the weak tunneling coupling is not a strict condition, but facilitates the technical treatment on the basis of sequential tunneling. Spin-polarized currents induced by a bias voltage lead to a finite polarization of the electron spin on the quantum dot. The electron spin can polarize the local magnetic moment $\boldsymbol{J}$ via the exchange coupling of strength q against an applied magnetic field and thus can lower its energy. At the same time, we study the average energy contained in the vibrational mode to monitor heating effects due to Ohmic losses. Energy exchange between the local magnetic moment $\boldsymbol{J}$ of the quantum dot and the vibrational mode is enabled via an effective magnetomechanical coupling. There are several examples of such couplings in both theory as well as experimental literature. Theoretical suggestions include interactions between a nanomechanical cantilever with a ferromagnetic tip on its surface [81], a nitrogen-vacancy (NV) impurity in diamond which couples to the magnetic tip

of a nanomechanical cantilever [82], single molecular magnets or nanoparticles mounted on doubly clamped nanobeams [83], or a single electron spin which couples to a flexural mode of a suspended carbon nanotube [84]. Experimental investigations of such systems were able to confirm magnetomechanical interactions. For example the coupling of the magnetic tip of a cantilever to an individual electron spin has been detected [78]. A clear sign of a magnetomechanical coupling has also been reported for a single NV center coupled to a SiC cantilever [42, 43]. Furthermore, a strong coupling between the magnetic moment of a single molecular magnet and a suspended carbon nanotube was demonstrated recently in Ref. [41].

More specifically, the quantum dot is modelled by a single electronic level with energy ϵ_0. The Coulomb repulsion U of electrons on the dot defines the charging energy. For small dots, the local charging energy exceeds all other energies, and a two-electron dot occupancy is energetically forbidden. The Hamiltonian can then be written as

$$H_d = \epsilon_0 \left(a_\uparrow^\dagger a_\uparrow + a_\downarrow^\dagger a_\downarrow \right) + \frac{g\mu_B}{\hbar} B s_z, \tag{26}$$

with the electron annihilation and creation operators a_σ and $a_\sigma^\dagger$, the g-factor g, and the Bohr magneton μ_B. The spin projection quantum number is σ and s_z the z-component of the electron spin $\boldsymbol{s} = \frac{\hbar}{2} \sum_{\sigma,\sigma'} a_\sigma^\dagger \boldsymbol{\sigma}_{\sigma\sigma'} a_{\sigma'}$. An external global magnetic field B splits the spin states along the quantization axis. A spin-1/2 impurity represents the local magnetic moment of the quantum dot. A generalization to higher spin values is possible, however, not pursued in this work. We denote with $J_z = \pm\hbar/2$ the projection of the local magnetic moment onto the quantization axis. The corresponding Hamiltonian for the dot's magnetic degree of freedom is given by

$$H_J = \frac{g\mu_B}{\hbar} B J_z + \frac{q}{\hbar^2} (\boldsymbol{s} \cdot \boldsymbol{J}), \tag{27}$$

where the electronic spin and the local magnetic moment $\boldsymbol{J}$ are coupled by an exchange interaction of strength q.

For simplicity, the exchange coupling is assumed to be isotropic. A single vibrational mode of frequency ω is coupled to the quantum dot in order to be able to study the dynamical heating and cooling of the device. With the bosonic ladder operators b and $b^\dagger$, the phonon Hamiltonian reads

$$H_{ph} = \hbar\omega b^\dagger b + \lambda \left(b + b^\dagger \right) \sum_\sigma a_\sigma^\dagger a_\sigma. \tag{28}$$

Due to the linear coupling of the electronic occupation to the oscillator position, it is possible to excite or relax the vibrational mode with each electronic tunneling process which populates the dot. These excitations describe the inevitable heating of the nanodevice due to the charge current. A relaxation of the phonon mode is possible if its energy exceeds the thermal energy of the ferromagnetic leads. The latter is the main mechanism used for passive heat sinks via the environment.

Energy exchange between the vibrational mode and the local magnetization is enabled by the magnetomechanical coupling given by

$$H_{J-\mathrm{ph}} = \frac{\xi}{\hbar}\left(b + b^\dagger\right)\left(J_+ + J_-\right) , \tag{29}$$

where $J_\pm = (J_x \pm iJ_y)/2$ are spin-1/2 ladder operators inducing transitions between the magnetic states with a simultaneous relaxation or excitation of the vibrational mode. It should be realized that equation (29) describes an effective coupling. Interactions between a vibrational mode and a spin can be the result of spin-orbit effects. Lehmann and Loss show in Ref.[85] that a combination of electron-phonon and spin-orbit interaction leads to an effective coupling between spin and phonons. By performing a Schrieffer-Wolff transformation [86], it is possible to eliminate the spin-orbit coupling in lowest order. A projection onto the orbital ground state then yields an effective spin-phonon coupling. In this way, all contributions from higher orbital states are neglected. The coupling constant ξ can then be derived as the ground state expectation value of a combination of electron-phonon operators and the generator of the transformation. Notice that the resulting coupling Hamiltonian as presented in Eq.(29) breaks time-reversal symmetry which could be restored by taking into account the higher orbital states for the electron. In this work, however, we will not focus on the origin or derivation of the magnetomechanical coupling. In order to explore the possibilities of a nanocooling mechanism, we use an effective description and choose both electron-phonon coupling λ and magnetomechanical coupling ξ independently.

A comparison with existing experimental setups yields experimental values for both coupling strengths. Ganzhorn et al. [41] have realized a set-up with a single molecular magnet covalently bound to a carbon nanotube suspended between two leads. The molecule has a magnetic ground state of $|\boldsymbol{J}| = 6$ and the groundstate doublet $J_z = \pm 6$ is separated from the excited states by several hundreds of Kelvin. A relaxation or excitation of the spin state therefore dominantly occurs via quantum spin tunneling between those two states. The Ising-like spin flip can therefore be described effectively by

a spin-1/2 impurity. The spin flip is accompanied by a transition in the vibrational mode and one finds the parameters [41] $\omega = 34$ GHz, $\xi = 1.5$ MHz, and $\lambda = \omega\sqrt{g} = 26$ GHz for $g = 0.6$, implying that $\xi/\omega \sim 4\times10^{-5}$ and $\lambda/\omega \sim 0.76$. The aforementioned experiments with NV centers [42] have a vibrational frequency of about $\omega = 2\pi \times 625$ kHz and a coupling strength of $\xi = g\mu_B \frac{\partial B}{\partial z}\sqrt{\hbar/(2m\omega)} \sim 172$ Hz, implying that $\xi/\omega \sim 4 \times 10^{-6}$. Another realization [43] yields $\omega = 2\pi \times 80$ kHz and $\xi \sim 8$ Hz, such that $\xi/\omega \sim 10^{-4}$.

The nanodevice is coupled to two ferromagnetic (FM) leads via tunnel coupling. In general, the magnetization directions of the leads can be noncollinear. They are modelled as non-interacting electron reservoirs

$$H_{\text{leads}} = \sum_{k\alpha\sigma} (\epsilon_{k\alpha} - \mu_\alpha)\, c^\dagger_{k\alpha\sigma} c_{k\alpha\sigma}, \tag{30}$$

where $c_{k\alpha\pm}$ represents the annihilation operator for an electron with the wave number k and the majority/minority spin in the lead $\alpha = L, R$ and $\mu_{L/R} = \pm eV/2$ is the chemical potential of the leads shifted by the applied bias voltage V. Ferromagnetic materials exhibit a different density of states at the Fermi energy for different spin species. If we define majority and minority spin carriers along the quantization axis of the quantum dot, we can quantify the polarization $p_\alpha = (\nu_{\alpha,+} - \nu_{\alpha,-})/(\nu_{\alpha,+} + \nu_{\alpha,-})$ of lead α by the relative difference in the density of states $\nu_{\alpha,\pm}$ for majority / minority spins at the Fermi energy. For the course of this chapter, we will use $p_L = p_R = p$. All energies are measured relative to the Fermi energy at zero polarization. The ferromagnetic leads induce an exchange field on the dot [28] which depends on the relative angle of the magnetization directions of the leads. Spin dynamical effects, which in turn affect the vibrational dynamics, are influenced by this field. Since we aim to cool the device by temporarily increasing the occupation of the spin groundstate, the source-lead polarization is chosen to be antiparallel to B. We consider three set-ups with the drain polarization parallel ($\downarrow\downarrow$), perpendicular ($\downarrow\rightarrow$) or anti-parallel ($\downarrow\uparrow$) to the source. To have an overall quantization axis, the tunneling Hamiltonian depends explicitly on spin rotation matrices as

$$H_t = \sum_{k,\alpha=L/R} \left[t_{k\alpha} A_\mu \Lambda^{(\alpha)}_{\mu\nu} C^\dagger_{\nu;k,\alpha} + \text{h.c.} \right], \tag{31}$$

with $A = (a_\uparrow, a_\downarrow)$, $C_{k,\alpha} = (c_{k\alpha+}, c_{k\alpha-})$ and $\Lambda^{(L)} = \Lambda^{(R,para)} = \mathbb{1}$, $\Lambda^{(R,anti)} = \sigma_x$ and $\Lambda^{(R,perp)} = (\mathbb{1} - i\sigma_y)/\sqrt{2}$ for the three setups. The hybridization with the dot state in the wide-band limit is given by $\Gamma_\alpha = 2\pi|t_{k\alpha}|^2(\nu_{\alpha,+} + \nu_{\alpha,-})$.

3.3. Energy Spectrum

In order to determine the spin and phonon dynamics of the system, we want to utilize the master equation and diagrammatic perturbation theory which we discussed in the previous chapter. By integrating out the leads one can obtain the master equation describing the time evolution of the reduced density matrix. Solving the master equation requires knowledge of the eigenvalues of the system Hamiltonian, $H_{sys} = H_d + H_J + H_{ph} + H_{J-\mathrm{ph}}$. A study of the eigenspectrum also demonstrates the effect of the electron-phonon interaction and helps to identify the spin groundstate for the local magnetization. In the limit of vanishing magnetomechanical coupling ($\xi \to 0$) an analytical diagonalization of the Hamiltonian is possible. To do so, we perform a polaron transformation [87]

$$\mathcal{U} = e^{\frac{\lambda}{\omega}(b^\dagger - b)\sum_\sigma a_\sigma^\dagger a_\sigma}. \tag{32}$$

The new system Hamiltonian reads

$$\mathcal{U} H_{sys}^{\xi\to 0} \mathcal{U}^\dagger = \left(\epsilon_0 - \frac{\lambda^2}{\omega}\right)\left(a_\uparrow^\dagger a_\uparrow + a_\downarrow^\dagger a_\downarrow\right) + \frac{g\mu_B B}{\hbar}\left(s_z + J_z\right) + \frac{q}{\hbar^2}\left(\boldsymbol{s}\cdot\boldsymbol{J}\right) + \hbar\omega b^\dagger b. \tag{33}$$

The impurity Hamiltonian H_J does not change under the polaron transformation. Consequently, we are left with an off-diagonal component of the Hamiltonian due to the exchange coupling q. For the magnetic degrees of freedom, we can find an eigenbasis formed by the singlet and triplet states of the two spin-1/2 moments of the electrons and the impurity. The eigenstates are listed in Table 1. Due to the polaron transformation, the energy of the electronic level is shifted by a factor λ^2/ω. Furthermore, electronic and vibrational degrees of freedom are no longer coupled in the system Hamiltonian. The interaction between electrons and phonons is transferred into the tunneling Hamiltonian by

$$\mathcal{U} a_\sigma \mathcal{U}^\dagger = e^{-\lambda/\omega(b^\dagger - b)} a_\sigma, \qquad \mathcal{U} a_\sigma^\dagger \mathcal{U}^\dagger = e^{\lambda/\omega(b^\dagger - b)} a_\sigma^\dagger. \tag{34}$$

Due to the transformation, we can now see clearly that each tunneling process yields the possibility to excite or relax the vibrational mode. The probability for such a process is given by an exponential function of the coupling strength λ relative to the eigenfrequency ω of the vibrational mode. For weak electron-phonon coupling, transitions to higher phonon states are therefore exponentially suppressed. Since the electron-phonon coupling is transferred into the tunneling Hamiltonian, we can now express the eigen-

Eigenstate	Energy
$\|0\uparrow\rangle$	$\epsilon_{0\uparrow} = B/2$
$\|0\downarrow\rangle$	$\epsilon_{0\downarrow} = -B/2$
$\|T^+\rangle = \|\uparrow\uparrow\rangle$	$\epsilon_{T^+} = \epsilon_0 - \lambda^2/\omega + q/4 + B$
$\|T^0\rangle = \frac{1}{\sqrt{2}}(\|\uparrow\downarrow\rangle + \|\downarrow\uparrow\rangle)$	$\epsilon_{T^0} = \epsilon_0 - \lambda^2/\omega + q/4$
$\|T^-\rangle = \|\downarrow\downarrow\rangle$	$\epsilon_{T^-} = \epsilon_0 - \lambda^2/\omega + q/4 - B$
$\|S\rangle = \frac{1}{\sqrt{2}}(\|\uparrow\downarrow\rangle - \|\downarrow\uparrow\rangle)$	$\epsilon_S = \epsilon_0 - \lambda^2/\omega - 3q/4$

Table 1: Eigenstates and corresponding energies for the electron-impurity subsystem in the case of vanishing magnetomechanical coupling.

basis of the system Hamiltonian via product states $|\chi\rangle = |\Phi\rangle|k\rangle$, where $|\Phi\rangle$ denotes the state of the subsystem formed by the electronic degrees of freedom and the local magnetization (impurity) and $|k\rangle$ denotes the state of the vibrational mode. The eigenstates of the electron-impurity subsystem with their respective energies are given in Table 1. The spin groundstate of the system can now be identified depending on the values for magnetic field B and exchange coupling q. We choose both the field as well as the coupling to be positive. The ground state can then be given by the empty dot and spin down impurity, the downwards polarized triplet state or the singlet. For strong exchange couplings compared to the magnetic field and electronic level ($q > 4\epsilon_0/3 + 3B/4$) the spin ground state is formed by the singlet $|S\rangle$. If the magnetic field is large compared to the electronic level and the exchange coupling ($B > 2\epsilon_0 + q/2$) the negative triplet state $|T^-\rangle$ has the lowest energy. In all other cases the spin ground state is given by the unoccupied dot with negatively polarized impurity spin $|0\downarrow\rangle$.

A diagonalization of the system Hamiltonian for finite magnetomechanical couplings $\xi \neq 0$ can be done numerically. The systems dynamics is then determined by the methods described in Chapter 2.3.4. The numerical effort for the solving the eigenvalue problem depends mainly on the dimension of the Hamiltonian. In this work, however, we want to utilize the vibrational mode as a means to monitor the temperature of the nanodevice. It is therefore necessary to keep all information about the state of the phonon mode. The dimension of the Hamiltonian then directly depends on the number K of phonon states taken into account, since we can not integrate out the vibrational degrees of freedom. K has to be large enough to provide a converging solution, yet at the same time should be held as small as possible in order to shorten the numerical calculations. Most of the results shown in this work are convergent with $K = 6$ phonon states. Calculations with a higher number of phonon states have shown corrections of

below one percent to the results presented in this work.

3.4. Principle mechanism

Before discussing the numerical results let us provide a qualitative understanding of the cooling scheme by explaining the principle mechanism. For the sake of this discussion, we will assume fully polarized leads in an anti-parallel configuration. The dot is empty, i.e., the number of electrons on the dot is zero, and the local magnetic moment $\boldsymbol{J}$ is in an excited state aligned parallel to an external magnetic field B along the dot quantization axis. As discussed in Chapter 2.2.2 the presence of ferromagnetic leads generates an effective magnetic field. In order to create an interaction between the electronic spin and the local magnetic moment, a noncollinear situation between the effective field and the external field is necessary. Due to thermal contact between the leads and the system, the vibrational mode is in a thermal state with the same temperature T as the ferromagnetic leads. A perfect polarization of the source lead anti-parallel to the dot quantization axis provides only spin-down electrons while the drain lead is polarized anti-parallel to the source along the quantization axis and therefore accepting only spin-up electrons. The cooling mechanism of the nanorefrigerator can then be explained by the following elementary processes (they are sketched in Figure 12):

- (I) Applying a finite bias voltage leads to spin-down electrons tunneling onto the quantum dot.
- (II) Due to the exchange coupling between the electronic spin and the local magnetization, a simultaneous flip of both spins is possible. The spin flip lowers the energy of the local magnetization.
- (III) With the drain being polarized anti-parallel to the source, the electrons can tunnel out of the dot only after such a spin flip, thereby lowering the overall current. Due to the electron-phonon coupling of strength λ, any tunneling event between dot and leads can lead to an excitation of the vibrational mode. These excitations represent a quantum analogy for Ohmic heating and increase the average energy of the vibrational mode over the thermal energy of the leads by a temperature ΔT_1. The energy of the vibrational mode, however, can be lowered due to the magnetomechanical coupling ξ.
- (IV) The vibration can relax when the magnetization is flipped from a low energy (spin down) into the high energy (spin up) state parallel to the external field,

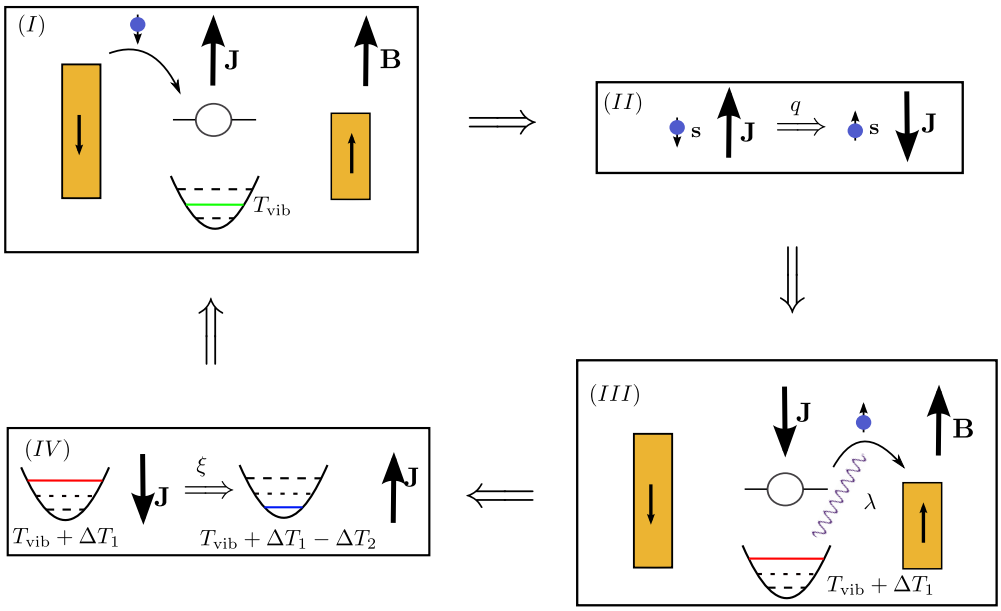

Figure 12: Schematic of the elementary processes for the nanorefrigerator. (I) Tunneling of an spin-down electron onto the quantum dot. (II) Simultaneous spin flip of electronic spin $\boldsymbol{s}$ and local magnetic moment $\boldsymbol{J}$ due to exchange coupling q. (III) The spin-up electron can leave the quantum dot. The tunneling process excites the vibrational mode by ΔT_1. (IV) The magnetomechanical coupling ξ induces spin flip of the local magnetic moment at the cost of vibrational energy. The new vibrational temperature is given by $T_{\mathrm{vib}} + \Delta T_1 - \Delta T_2$.

thereby reducing the vibrational temperature by ΔT_2. The energy stored in the magnetization can then again be removed by interaction with the spin of the next tunneling electron as symbolized in (I) thus leading to a net cooling effect of the vibrational mode.

An important component for a cooling effect is the ratio between the Ohmic heating ΔT_1 induced by the electronic current and the removal of heat ΔT_2 due to spin flips. Furthermore, the polarization of the local magnetic moment by the electronic spin plays an important role. The efficiency of the cooling protocol can therefore depend on the lead polarization, the polarization directions, the electron-phonon coupling and magnetomechanical coupling strengths, and the energy difference between the high- and the low-energy spin state induced by the external field B.

3.5. Preparation

In order to be able to quantify a cooling effect, it is necessary to both define an effective temperature for the vibrational degrees of freedom of the system as well as to prepare the system in a suitable initial state. The stationary solution of the Markovian quantum master equation does not depend on the initial state of the system. We are, however, interested in the spin and the phonon dynamics of our system. The time evolution of the density matrix explicitly depends on the initial state. While choosing an arbitrary preparation similar to what we chose to describe the principle mechanism might yield a meaningful time evolution, it might very well lead to misleading results with respect to the cooling efficiency of the nanorefrigerator. Let us revise this with two extreme examples. Imagine the device to be prepared in such a way that the vibrational mode is in its ground state. In this case, the vibrational temperature is at a minimum which makes further cooling of the vibrational degrees of freedom impossible. Similarly, if we prepare the system in a highly excited state we start with a high vibrational temperature. If the initial vibrational temperature is higher than the temperature of the ferromagnetic leads, a cooling effect will occur due to the thermal contact between the device and the environment. This cooling effect however does not differ from the mechanism used in passive cooling devices as mentioned previously. Our aim is to investigate the viability of the dynamical demagnetization cooling on the nanoscale via spin-polarized currents. A suitable preparation can be found by placing the nanodevice in thermal equilibrium with the leads. In this way, passive cooling effects can be ruled out and a decrease of the effective temperature below this initial preparation will show the viability of a dynamic

cooling scheme. Such a preparation can be realized numerically by calculating the stationary solution of the master equation for the system in contact with the ferromagnetic leads but without a bias voltage, $eV = 0$.

For a quantitative analysis of the cooling mechanism, we need to define the effective vibrational temperature of the system. The model system we have chosen includes a single vibrational mode to represent the thermal state of the system. Relaxation and excitation of the phonon mode out of its initial state reflects cooling and heating processes and is possible via the electron-phonon coupling and the magnetomechanical coupling. The average energy of the vibrational mode can therefore serve as a measure of the vibrational temperature of the nanorefrigerator according to

$$T_{\text{eff}} = \langle H_{ph} \rangle / k_{\text{B}}. \tag{35}$$

In principle, there are several ways to define an effective temperature via the phonon energy. Phonon operators appear in the magnetomechanical coupling term, the electron-phonon coupling and the Hamiltonian for the harmonic oscillator. A numerical comparison between different definitions of the phonon temperature including and excluding both couplings λ and ξ shows no significant differences. We chose to include the electron-phonon coupling into the definition while we exclude the magnetomechanical coupling. The initial effective temperature will be denoted by $T_{\text{init}} = T_{\text{eff}}(t = 0)$. In Figure 13, we see the initial vibrational temperature as a function of the lead temperature. The effective temperature defined by the energy of the vibrational mode fits very well with the mean thermal energy of a harmonic oscillator

$$\langle E_{\text{harm}} \rangle = \frac{\sum_{k=0}^{K} \hbar\omega k e^{-\beta\hbar\omega k}}{\sum_{k=0}^{K} e^{-\beta\hbar\omega k}}, \tag{36}$$

at the lead temperature T denoted by the red data points in Figure 13. Any deviation between the two energies is caused by the electron-phonon and the spin-phonon coupling, since the preparation of the system includes all couplings and the ferromagnetic leads. The coupling strengths however are at least one order of magnitude smaller than the energy scale given by the electronic and vibrational levels, thus resulting in no significant differences between the two curves.

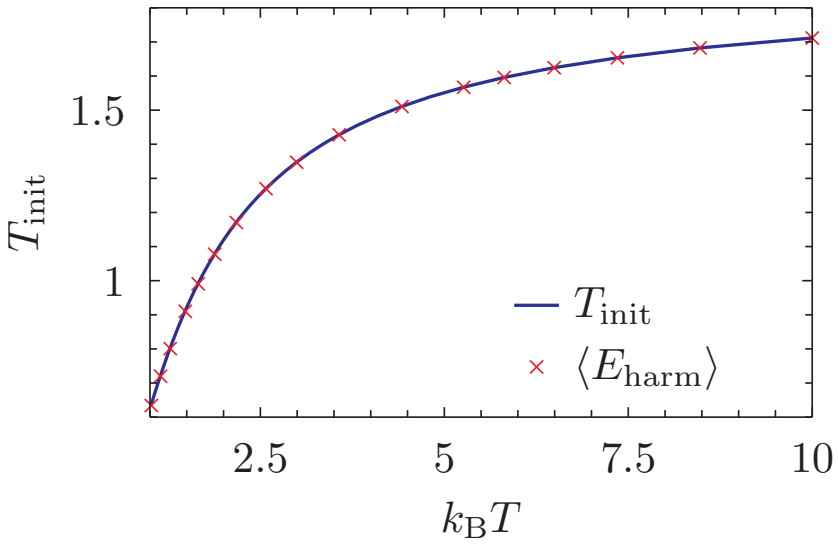

Figure 13: Initial effective temperature $T_{\rm init}$ (black solid line) and mean thermal energy of a free harmonic oscillator (red crosses) as a function of the lead temperature T. The numerical parameters are: $\epsilon_0 = 1$, $\hbar\Gamma = 0.01\epsilon_0$, $p = 0.9$, $q = 0.4\epsilon_0$, $\hbar\omega = 0.75\epsilon_0$, $\xi = 0.06\epsilon_0$, $\lambda = 0.2\epsilon_0$, $B = 0.7\epsilon_0/(g\mu_B)$, $K = 6$ and $eV = 0$.

3.6. Effective Cooling

The next important step after preparing the initial state is to find suitable parameters for a cooling protocol. The parameters of the problem can be guided by using numerical convenience and our expectations for efficient cooling. Due to the sequential tunneling approximation in the master equation, we are forced to consider weak system-lead coupling only. The tunnel coupling Γ will therefore be the smallest energy of the problem. The energy of the electronic level serves as a scaling parameter for all other energies. Temperature T, phonon frequency ω and bias voltage eV can be chosen to be on the same order of magnitude as the electronic level. Furthermore, we will choose a rather strong magnetic field B of the same magnitude in order to generate a large splitting between the magnetic ground and excited state. This energy splitting corresponds to the amount of heat we can transfer between the magnetic and the vibrational degrees of freedom via a spin flip induced by the magnetomechanical coupling ξ. The coupling strengths λ and ξ are chosen to be one or two orders of magnitude smaller. The electron-phonon coupling λ has to be small enough to allow the numerical calculations to reach convergence within a reasonable amount of time. On the other hand it still has to be sufficiently strong to observe signatures of the electron-phonon interaction and heating effects. The magnetomechanical coupling ξ should typically be smaller or at most of the same order of magnitude as is suggested by the experimental values listed in Sec. 3.2. Here we will choose on purpose a rather large ξ to demonstrate the cooling effect.

Another important set of parameters for the cooling setup consists of the lead polarizations and alignments. Both the magnitude as well as the direction of the lead polarization will have a significant effect on the cooling efficiency of the setup since, they directly control the spin and lifetime of electrons on the quantum dot [28]. Consequently, they affect the local magnetization via the exchange coupling. To develop an efficient cooling protocol we therefore compare different setups for the ferromagnetic leads. We investigate the spin accumulation, current, number of electrons on the dot, and the effective phonon temperature for the three different lead setups which were introduced in Section 3.2: A parallel alignment ($\downarrow\downarrow$) of the source and drain polarization, a perpendicular alignment ($\downarrow\rightarrow$) and an anti-parallel alignment ($\downarrow\uparrow$).

Parallel Setup

The parallel setup ($\downarrow\downarrow$) is marked by the black dashed lines in Figures 14-17. Here, electrons carrying a majority spin are able to tunnel through the quantum dot without

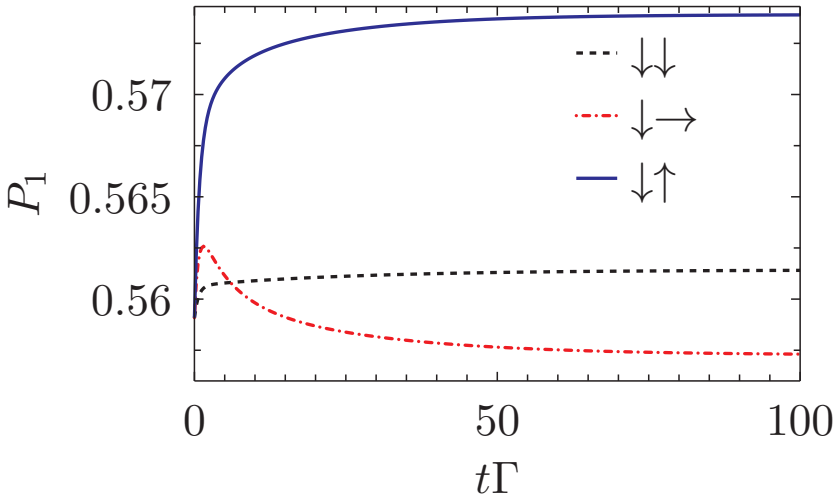

Figure 14: Probability P_1 to find an electron on the quantum dot as a function of time for all three lead setups. The applied bias voltage is $eV = 1.2\epsilon_0$. The remaining parameters are the same as in Figure 13.

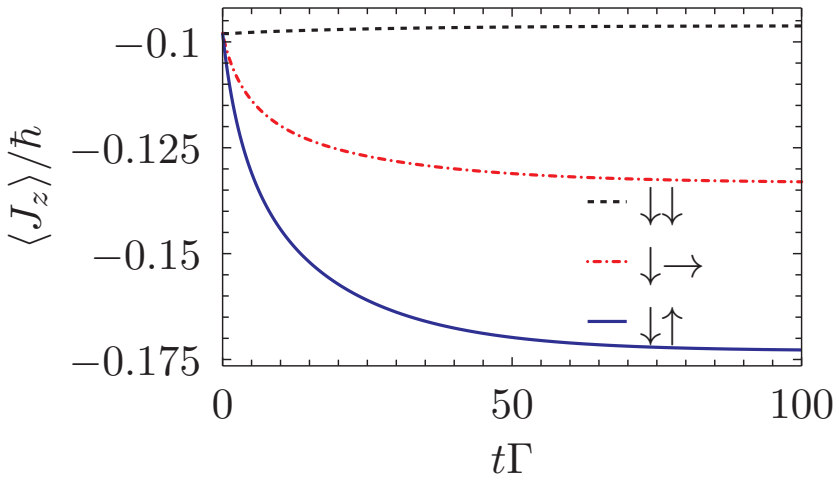

Figure 15: Average z-component $\langle J_z \rangle$ of the magnetization of the quantum dot as a function of time for all three lead setups. The parameters are the same as in Figure 14.

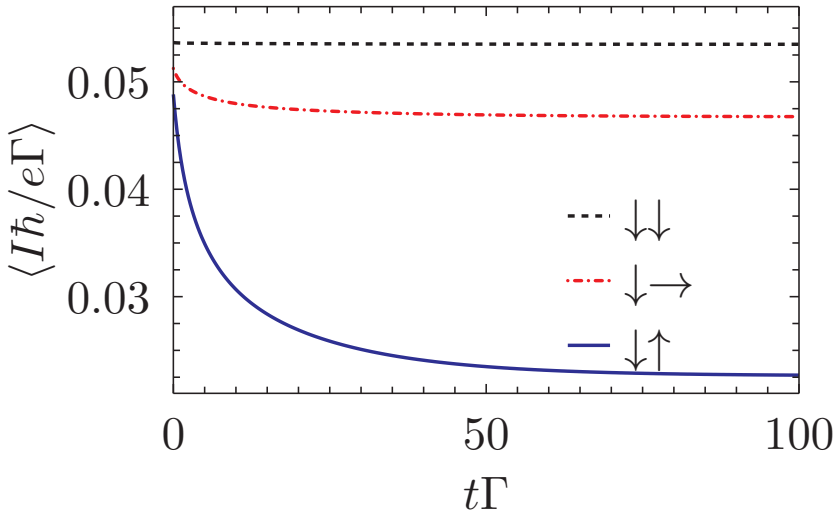

Figure 16: Charge current $\langle I \rangle$ as a function of time for three different lead setups. The parameters are the same as in Figure 14.

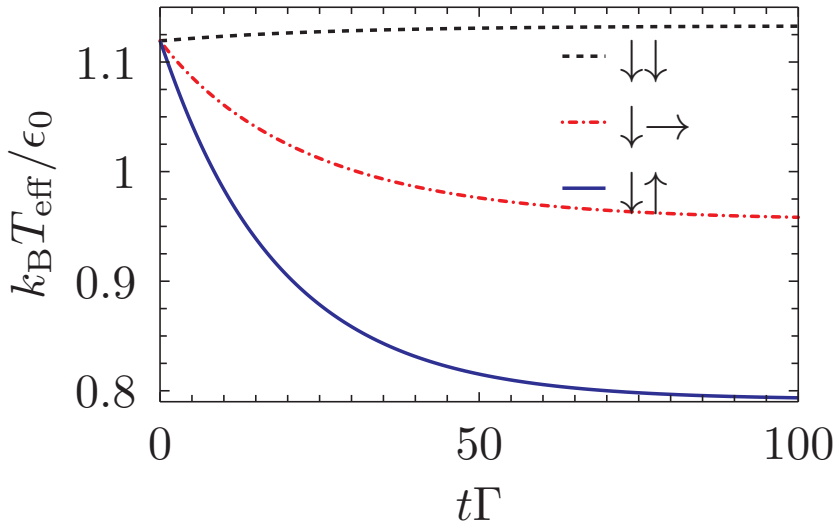

Figure 17: Effective vibrational temperature T_{eff} as a function of time for three different lead setups. The parameters are the same as in Figure 14.

the necessity for a spin flip. Thus, no spin blockade occurs and the electrons tunnel through the quantum dot mostly without interacting with the local magnetization $\boldsymbol{J}$. We therefore expect an average occupation number of the quantum dot of about $1/2$ and a weakly polarized local magnetization anti-parallel to the dot quantization axis. This clearly can be seen in Figure 14 and Figure 15, respectively. Even though the average occupation P_1 of the quantum dot is close to the other setups, the individual lifetime of each electron on the dot is rather short. Proof of this can be seen in the charge current depicted in Figure 16. As a result of the rather large current in the steady state we expect a relatively large influence of Ohmic heating effects. Each transfer of an electron between the quantum dot and the ferromagnetic leads has a finite probability of exciting the vibrational mode. Free charge transport through the quantum dot can therefore be expected to result in a fast heating of the vibrational mode as compared to a regime where the current is blocked. Simultaneously, due to the weak interaction with the magnetic impurity, spin flips are unlikely to happen, thus reducing the efficiency of the cooling mechanism. Consequently, the effective vibrational temperature of the nanodevice is slightly increasing with time and no cooling effect can be observed (see Figure 17).

Perpendicular Setup

The red dotted-dashed lines in Figures 14-17 show the results for perpendicularly aligned lead polarizations ($\downarrow\rightarrow$). The different density of states in source and drain lead for majority and minority spin carriers causes a suppression of the current shown in Figure 16. A spin blockade occurs. The electrons are trapped on the quantum dot and need to precess or exchange angular momentum with the local magnetization in order to tunnel into the drain lead. Signatures of spin-spin interactions can be found in the polarization of the local moment J_z depicted in Figure 15. A significant increase in the polarization and therefore a decrease in the magnetic energy can be observed. At the same time the average occupation of the quantum dot decreases with the magnetic moment (see Figure 14). The combination of these effects leads to a sizeable decrease in the effective temperature of the vibrational mode shown in Figure 17.

Anti-parallel Setup

The blue solid lines in Figure 14-17 depict the anti-parallel configuration ($\downarrow\uparrow$). An optimal polarization of the local magnetic moment can be found here. The anti-parallel setup shows a larger average occupation of the quantum dot as compared to the other two setups. Due to the opposite spin carrier distributions in the leads, a strong spin

blockade is formed trapping the electrons on the device. Figure 14 shows the mean occupation number. This generates a strong polarization of the local magnetic moment (see Figure 15). The trapped electrons can only leave the quantum dot by flipping their spin simultaneously with the local moment. These spin flips lead to a decrease of the vibrational temperature and provide a strong cooling effect as shown in Figure 17.

The ↓↑-setup is shown to be optimal in two respects. First the polarization of the magnetic moment is enhanced by the long lifetime of the electrons on the dot resulting in a low magnetic energy of $\boldsymbol{J}$ compared to the other two setups. Second, the spin blockade forces the electrons to exchange angular moment with the local magnetic moment. The vibrational energy decreases in the process. In a fully polarized case, every transmitted electron will contribute to the cooling process. Additionally, the Ohmic heating effects are directly connected to the charge current and therefore suppressed. This significantly improves the cooling efficiency. In Figure 16, we see that the charge current is significantly lower than in the other two setups. We can conclude that the (↓↑) alignment is optimal for the purpose of our cooling procedure. For the chosen parameters we can report a decrease of the effective temperature as compared to its initial value for both the anti-parallel as well as the perpendicular setup. We have thus already provided a proof of principle for the nanocooling scheme we proposed.

Dependence on the bias voltage

Figure 18 shows the steady state limit of the effective vibrational temperature as function of the bias voltage eV for the three lead setups. The results agree very well with the results of our investigation of the spin and phonon dynamics in Figures 14 to 17. No discontinuous behaviour of the effective temperature for small or large bias voltages is observed in any of the setups. For the perpendicular and anti-parallel lead setup we observe decreasing temperatures for positive bias voltages and increasing temperatures for larger, negative bias voltages. This effect is a result of the asymmetric polarizations of the ferromagnetic leads. For negative bias voltages spins are injected into the quantum dot from the drain lead and not the source lead. The localized magnetic moment of the quantum dot is therefore polarized in a different direction compared to positive bias voltages, leading to an increase of the effective temperature of the vibrational mode. For the parallel lead setup no such effect can be observed since both source and drain lead are polarized in the same direction. In the following we will focus on the anti-parallel alignment in order to further investigate the efficiency of the cooling scheme.

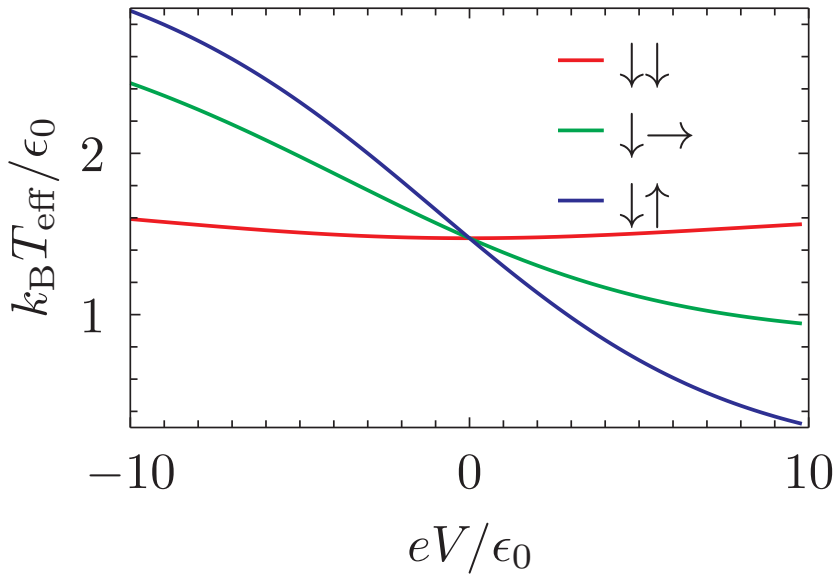

Figure 18: Steady state solution of the effective vibrational temperature as a function of the applied bias voltage for all three lead setups. The numerical parameters are the same as in Fig 14.

Role of the electron-phonon and magnetomechamical coupling

The ratio of T_{eff} and the initial temperature T_{init} as a function of the electron-vibration coupling λ and the magnetomechanical coupling ξ is displayed in Figure 19. A cooling effect is achieved in the full parameter regime depicted. In agreement with our expectation, an increase of the electron-phonon coupling λ leads to an increase of the effective vibrational temperature as the result of Ohmic heating (see Figure 20 (a)). The heating effects are however outmatched by the magnetization cooling as long as the strength of the magnetomechanical coupling ξ is of the same order of magnitude as the electron-phonon coupling. Surprisingly, for a fixed λ, a nonmonotonic dependence of the cooling as a function of ξ can be observed as shown in Figure 20 (b). For small couplings T_{eff} steadily decreases with increasing ξ. However, a minimum is reached where cooling is optimal. For further increasing ξ, the effective vibrational temperature increases again. The energy spectrum of the system without spin-phonon interactions is given in Sec.3.3. Finite values for ξ will lead to corrections of the calculated eigenenergies and can lead to a change of the magnetic ground state. Since the cooling scheme relies on a polarization of the local magnetic moment to the magnetic groundstate, large values for ξ can therefore decrease the cooling efficiency.

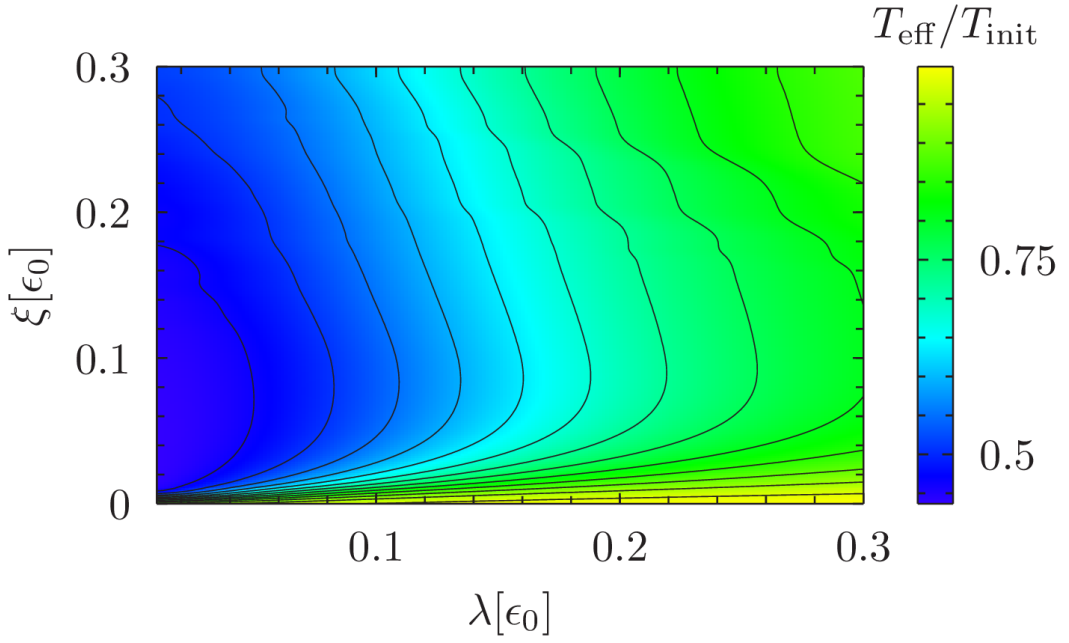

Figure 19: Effective vibrational temperature $T_{\rm eff}$ in the stationary limit versus electron-phonon coupling λ and magnetomechanical coupling ξ. The remaining parameters are the same as in Fig 14.

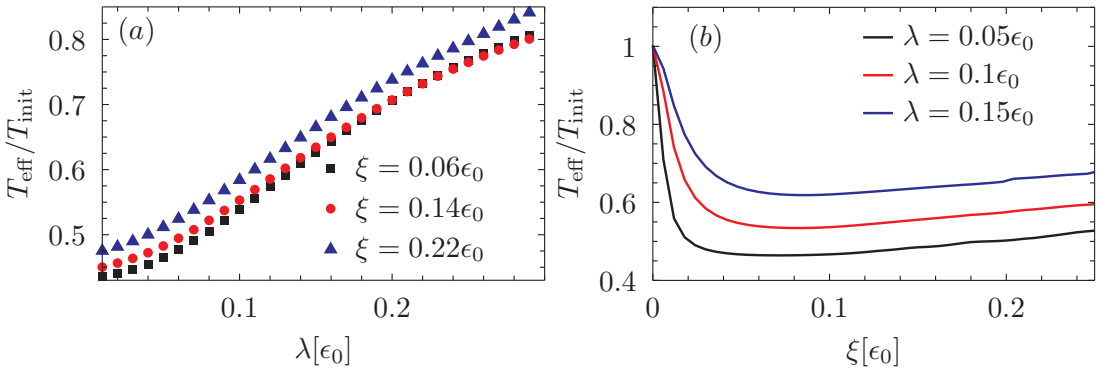

Figure 20: Horizontal (a) and vertical (b) cuts through Figure 19. The cuts show the effective vibrational temperature as a function of the electron-phonon coupling λ and the magnetomechanical coupling ξ, respectively. The remaining parameters are the same as in Fig 19.

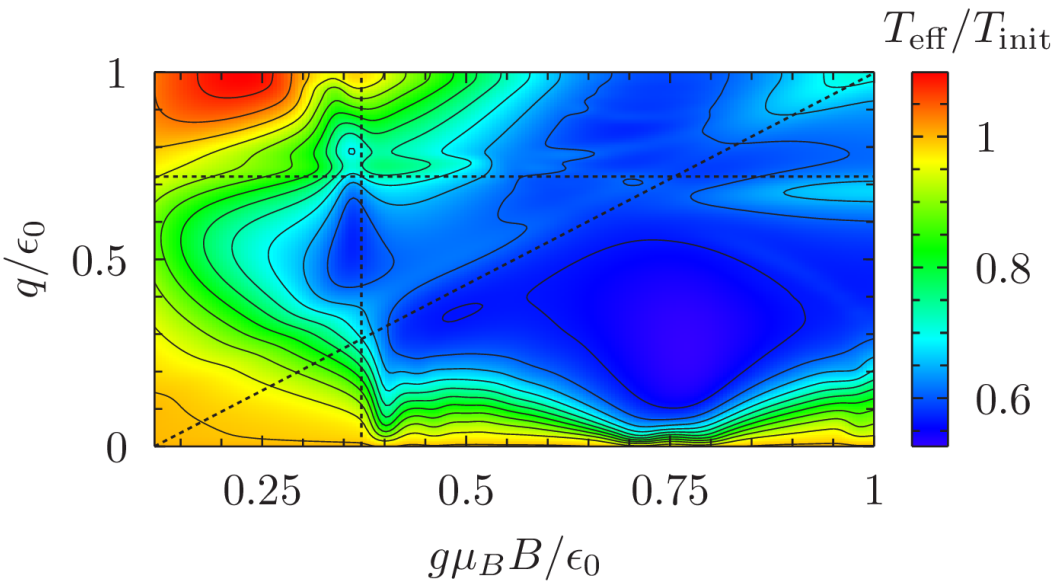

Figure 21: Effective vibrational temperature $T_{\rm eff}$ in the stationary limit versus magnetic field $g\mu_B B$ and spin-magnetization exchange coupling q. The dashed lines denote resonances between spin flips and vibrational transitions in the noninteracting limit. The remaining parameters are the same as in Fig 14.

Influence of the magnetic field and exchange coupling

In Fig 21, the steady state limit of $T_{\rm eff}$ is shown as a function of the magnetic field $g\mu_B B$ and the spin-magnetization exchange coupling q. The cooling effect is more pronounced for higher magnetic field since the energy gain due to the spin polarization is proportional to the magnetic field. A strong exchange coupling changes the magnetic groundstate similar to the previously discussed effect for the magnetomechanical coupling. The efficiency of the cooling protocol however directly depends on the energy necessary for a spin flip. A change of the magnetic groundstate can lower this energy and therefore decrease the amount of heat extracted from the vibrational mode with each spin flip. Additional fine structures can be observed due to resonances between spin flips and vibrational transitions. Since the magnetomechanical coupling is small ($\xi = 0.06\epsilon_0$), we can give an analytic approximation for these resonances in the noninteracting limit ($\xi \to 0$). The dashed lines in Figure 21 indicate these resonances using the eigenenergies given in Table 1. The states $|T^+\rangle$ and $|T^-\rangle$ are split by an energy difference $\Delta\epsilon = 2B$. For the states $|T^0\rangle$ and $|S\rangle$ the energy difference equals $\Delta\epsilon = q$.

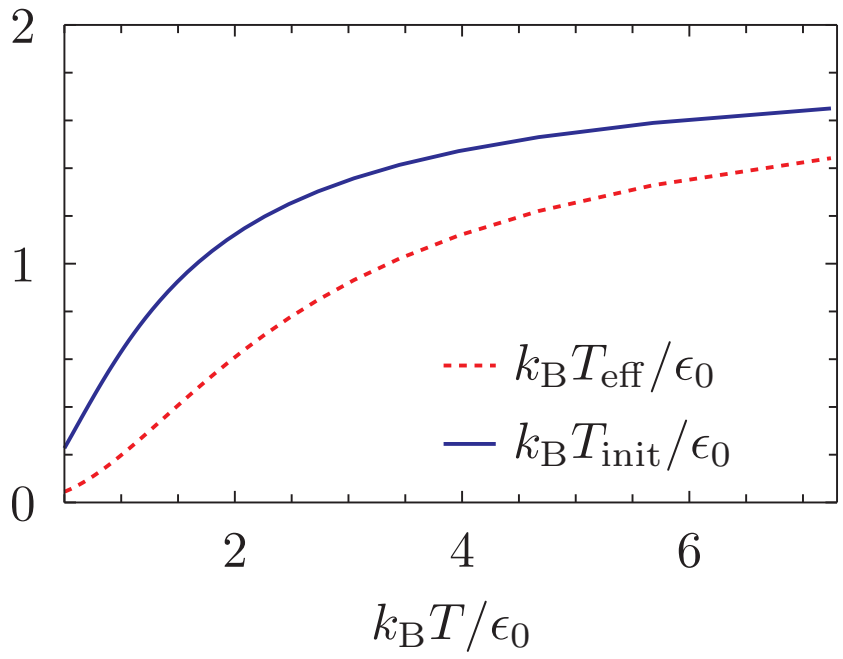

Figure 22: Effective vibrational temperature in the initial, thermalized state ($T_{\text{init}}, V = 0$) and in the final steady state ($T_{\text{eff}}, V > 0$) as a function of the lead temperature T for $\xi = 0.12\epsilon_0$ and $\lambda = 0.1\epsilon_0$. The remaining parameters are the same as in Fig 14.

A resonance occurs whenever these energy differences are equal to the frequency of the vibrational mode. These two cases are indicated by the horizontal and vertical dashed lines. Finally, when $B = q$ we find that the states $|T^-\rangle$ and $|S\rangle$ are degenerate. This case is indicated by the third dashed line in Figure 21.

To further demonstrate the cooling effect we show the final and initial effective temperature as a function of the lead temperature in Figure 22. We observe that for all depicted values of the lead temperature T, the effective vibrational temperature in the steady state limit is lower than its initial value. A cooling effect can be maintained for a range of at least one order of magnitude of the lead temperature. The initial temperature is not directly proportional to the lead temperature. This is the result of the preparation of our setup and the definition of the effective temperature as can be seen in Figure 13 where we compare it with the average energy of a harmonic oscillator.

Cooling rate

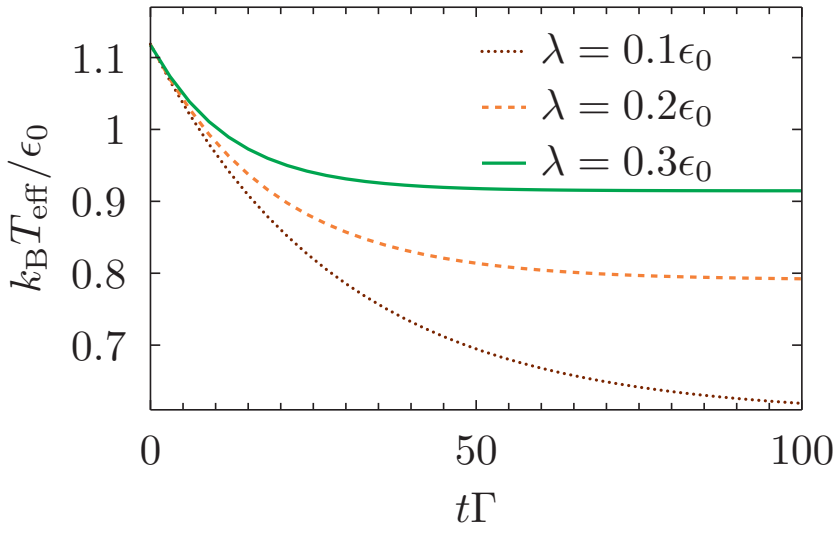

Figure 23: Effective vibrational temperature T_{eff} versus time for different electron-phonon coupling strengths λ. The parameters are the same as in Figure 14.

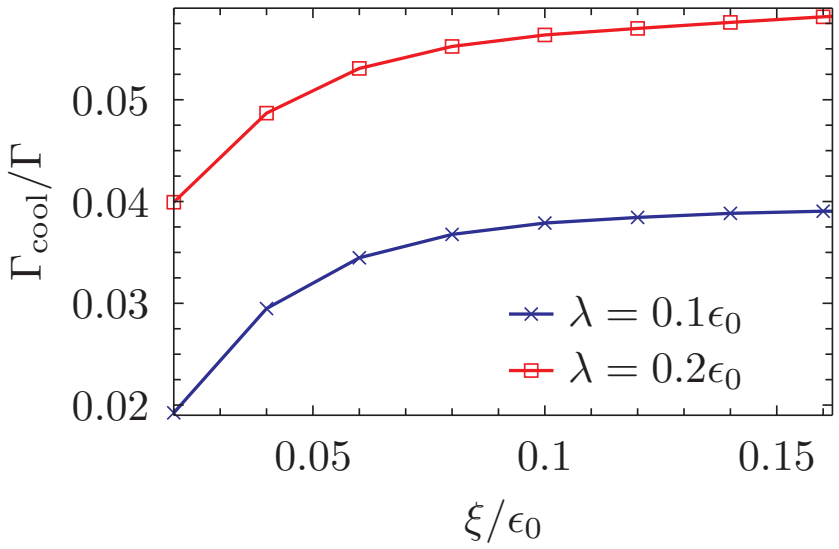

Figure 24: Vibrational cooling rate Γ_{cool} versus the magnetomechanical coupling ξ for two different electron-phonon couplings $\lambda = 0.1\epsilon_0$ and $\lambda = 0.2\epsilon_0$. The remaining parameters are the same as in Fig 14.

A useful measure for the efficiency of a cooling protocol is not only the maximum achievable cooling effect, but also the speed at which the temperature is reduced. We can define an effective temperature as in Eq. (35) at all times. Comparing the time evolution of the effective temperature in the anti-parallel lead setup for different values of the electron-phonon couplings, we find an exponential approach to the steady-state as show in Figure 23. Since the vibrational temperature (see Eq.(35)) is defined by the average energy of the vibrational mode, it depends directly on the relaxation dynamics of the vibrational states. In Chapter 2.3.4, we have seen that the master equation can be solved by an exponential function. The exponent is given by the Redfield rates and the coherent oscillations of the system. The relaxation dynamics is described by the real part of the Redfield rates. Therefore, an exponential approach of the steady-state solution results. An effective cooling rate Γ_{cool} can therefore be determined by a fit to our numerical results according to

$$T_{\mathrm{eff}}(t) \simeq T_{\mathrm{eff}}(\infty) + e^{-\Gamma_{\mathrm{cool}} t}(T_{\mathrm{init}} - T_{\mathrm{eff}}(\infty)). \tag{37}$$

In Figure 24, we show the cooling rate versus the magnetomechanical coupling for two values of the electron-vibration coupling λ. An initial strong increase of the cooling rate with increasing ξ can be observed. However, for $\xi \gtrsim 0.1$ the cooling rate saturates. This result is in agreement with our remarks on the observations made in Figure 21.

Dependence on the lead polarization

Naturally the effectivity of the cooling scheme depends on the degree of polarization of the ferromagnetic leads. In Figure 25 we show the effective temperature of the device compared to its initial value as a function of the lead polarization p. In Figure 25 (a) we see the results for the anti-parallel setup ($\downarrow\uparrow$) which we have used so far to induce an injection of spin-down electrons into the nanodevice. The cooling effect scales linearly with the polarization of the FM leads as long as a magnetomechanical coupling is present. As expected, there is no change in the vibrational temperature to be observed for vanishing coupling. By reversing the polarization of the leads it is also possible to transform the nanorefrigerator into a nanoheater as shown in (b). The source lead then provides spin-up electrons which polarize the local magnetic moment into an excited state. The magnetomechanical interaction can then only induce spin flips which lower the magnetic energy. The excess energy of such a process is then transferred into the vibrational mode which leads to an increase of the effective temperature.

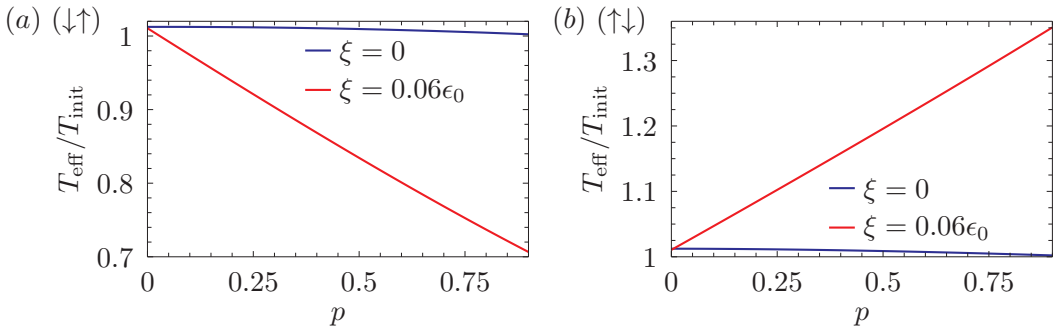

Figure 25: Effective vibrational temperature of the nanodevice as a function of the lead polarization p for both finite (red line) and vanishing (blue line) magnetomechanical coupling. The leads are aligned anti-parallel with the source lead being polarized anti-parallel to the dot quantization axis in (a) and parallel to the quantization axis in (b). The remaining parameters are the same as in Figure 14.

Asymmetric tunneling barriers

Finally, we can manipulate the effective temperature by changing the lead couplings. So far, we have assumed symmetric tunnel couplings $\Gamma_L = \Gamma_R$ between the quantum dot and the ferromagnetic leads. The rate for transitions between the nanodevice and the ferromagnetic leads to first order in the system-lead interaction are essentially given by Fermi's Golden rule [88, 89] and therefore directly depend on the coupling strength Γ. Reducing the tunnel coupling between the nanodevice and the drain lead will thus lead to an overall increase of the lifetime of electrons on the dot by suppressing the the transition probability. This in turn leads to a stronger polarization of the local magnetization which will lead to an increase of the cooling effect. Figure 26 shows the effective temperature as a function of time for the parallel and the anti-parallel lead setup with asymmetric lead couplings. Compared to Figure 17 we do not observe any major changes for the anti-parallel setup since the life time of electrons on the dot is mainly determined by the spin blockade. For the parallel setup, however, we do observe a decrease of the effective temperature for times smaller than $t\Gamma \simeq 100$. Previously, with symmetric lead couplings, we could not observe any cooling when the lead polarizations where aligned parallel to each other. Increasing the tunnel barrier between quantum dot and drain however traps the electrons on the quantum dot and yields a decrease of the vibrational temperature. Establishing a dynamical cooling protocol is therefore

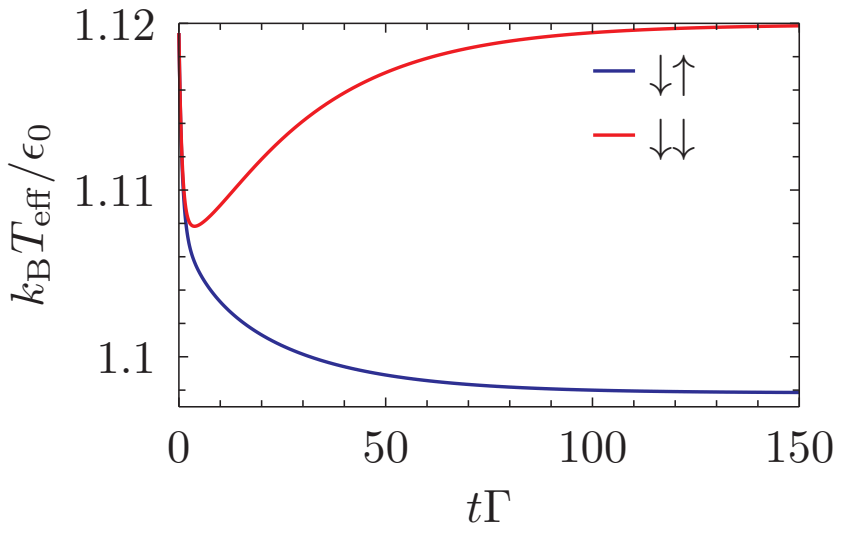

Figure 26: Effective vibrational temperature as a function of time for the anti-parallel and parallel lead setup. The system lead couplings are chosen to be asymmetric with $\Gamma_L = 0.005 = 100\Gamma_R$. The remaining parameters are the same as in Figure 14.

possible even with parallel lead alignments, however, under the condition of asymmetric tunnel barriers.

3.7. Conclusion

We have proposed a cooling mechanism for a magnetic nanodevice based on spin-polarized currents and magnetomechanical interactions. By establishing a simple model using ferromagnetic leads and a magnetic quantum dot, we are able to investigate the viability of the proposed cooling scheme. We find that an anti-parallel alignment of the source and drain lead polarizations leads to a spin-blockade and therefore an accumulation of spin on the nanodevice. The resulting low charge current and strong polarization of the magnetic quantum dot turn out to be optimal for our cooling proposal. The cooling induced by the magnetomechanical coupling overcompensates Ohmic heating effects due to electron-phonon interactions. We find a cooling effect for a wide range of parameters yielding a decrease of the effective vibrational temperature of the nanodevice up to 50% of the initial value. Surprisingly, a decrease of the cooling effect can be observed for stronger magnetomechanical couplings. Accordingly, we find that the cooling rate saturates as a function of the magnetomechanical coupling, implying

that not very strong couplings are required to observe the proposed effect. By reducing the strength of the tunnel coupling between the nanodevice and the drain lead a temporary spin accumulation can be achieved even in the parallel lead configuration. We report that, in this case, a dynamic cooling of the vibrational mode is possible with a strong asymmetry of the tunnel couplings. Finally, be reversing the polarization of the ferromagnetic leads, we are able to utilize the mechanism of the cooling protocol to build a nanoheater.

4. Spin-polarized Transport through vibrating Molecules

Measurements of magnetic and electronic properties of molecules are often performed by placing the sample molecule on a metal substrate. The contact with the metal substrate, however, can lead to chemical reactions and specifically to a strong hybridization of the sample molecule. This hybridization yields a significant change in the molecule's characteristics such as the orbitals, i.e., the energy spectrum, and the magnetic moment of the molecule. If a molecule is investigated in order to determine its use as a single molecule transistor or similar nanodevice we are, however, interested in learning the characteristics of the molecule without hybridization between the molecular electronic states and those of the substrate. Such a situation can be achieved experimentally by placing the sample molecule on a non-reactive surface such as a graphene layer. The graphene layer itself can then be placed on top of a magnetic material in order to provide a ferromagnetic charge reservoir. A setup like this has been realized by M. Bazarnik and J. Brede at the university of Hamburg and is schematically shown in Figure 27. In the following, we investigate this situation in terms of a theoretical model. We adress spin-polarized transport in an Anderson-Holstein model. In Section 4.1 the experimental setup is explained and the experimental results are discussed. On the basis of these results and the setup, we formulate a model for the theoretical investigation in Section 4.2. A comparison between the experimental and theoretical results is made in Section 4.3. In Section 4.4, we determine the effective field induced by the ferromagnetic leads in order to gain further insight into the experimental results. The differences between non-equilibrium and equilibrium phonon modes are addressed in Section 4.5. Finally, we conclude by summarizing the results in Section 4.6.

4.1. Experiment

In order to avoid a strong hybridization of a sample molecule and its underlying host substrate as part of the experimental preparation, it is necessary to place the molecule on a non-reactive surface. Spectroscopic methods such as the scanning tunneling microscopy can then be used to determine the electronic properties of the sample. This is the core idea of the experiment conducted by M. Bazarnik and J. Brede. A scheme of the experimental setup is shown in Figure 27. The sample molecule is composed of Phthalocyanine with a single cobalt or copper atom as a metal center (see Figure 28, left side). This molecule is suitable for an experimental investigation for several reasons. First, it is very stable with respect to temperature allowing to conduct experiments even

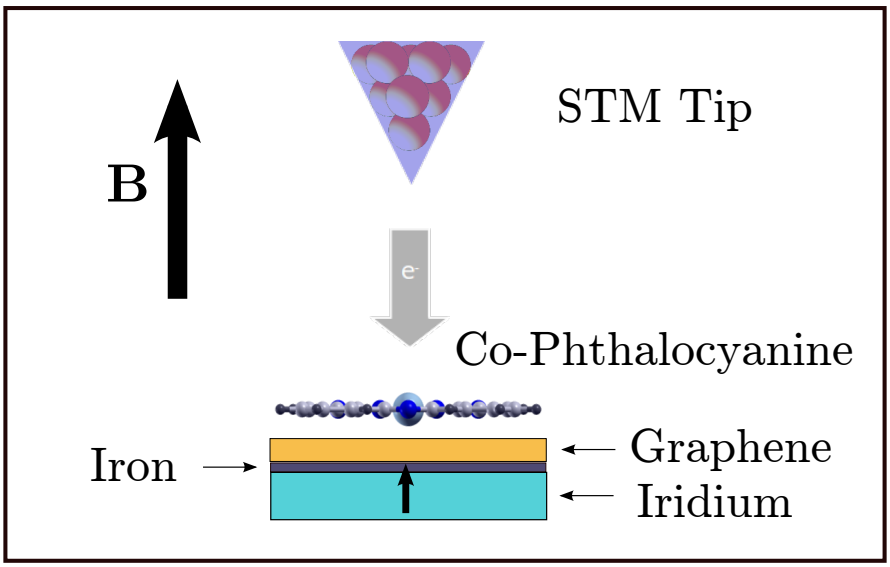

Figure 27: Schematic of the experimental setup. The sample molecule (CoPhthalocyanine) is placed on top if a graphene layer. An iron layer between the graphene and the iridium bulk of the substrate induces a strong magnetic moment. An external field $\boldsymbol{B}$ is used to polarize the tip of the scanning tunneling microscope.

without a complicated cooling setup. Second, the molecule is flat which simplifies both measurements as well as a preparation of sample on top of the substrate. The combination of those two characteristics makes it an optimal candidate for STM studies. The molecule is placed on a graphene layer. The graphene is placed on top of a thin iron layer which in turn is on top of a 111-iridium monocrystal. The iron layer induces a strong magnetic moment in the substrate creating a hard magnet while the graphene prevents any direct interactions between sample and substrate.

The experimental setup is completed by the scanning tunneling microscope. Such a microscope can be used to determine the surface structure of sample and substrate as well as the current-voltage characteristics of the sample molecule. For our studies the most important part of the microscope is the tip. The tip is sharp and consists of tungsten coated with an iron film of about 50nm thickness, making it a soft magnet. Placing the tip in the vicinity of the sample and applying a voltage creates a tunnel contact which allows to send a charge current through the molecule. The finite spin polarization of both the STM tip and the substrate allows for spin sensitive measurements. An external magnetic field B is applied in order to be able to switch the polarization of the tip. The scanning tunneling microscope can be operated in two modes. The first mode is used to acquire a surface picture of the sample and the substrate. To do so, the voltage applied between the tip and the substrate is kept constant. While sweeping over the surface of the substrate, the distance between the tip and the surface can be adjusted in such a way that the measured current is kept constant as well. The adjusted distance as a function of the tip position then generates a picture of the surface topology as shown in Figure 28 on the right side.

The surface scans can then be used to position the STM tip over one of the molecule centers. At this point the second measurement mode can be utilized to perform a spectroscopy of the molecule. By disabling the feedback loop, the distance between tip and surface can be fixed allowing a measurement of the current as function of the applied bias voltage. Using a lock-in device directly yields the differental conductance (dI/dV) and leads to a reduction of the ratio of noise and signal. Figure 29 shows the experimental results averaged over a series of measurements over the center of Cobalt-Phthalocyanine for two different values of the external magnetic field. Notice that the experimental results are rescaled by a factor α.

The data shows a series of peaks in the differental conductance with changing magnitude and ratio between neighbouring peaks for the two different directions of the external field. We can identify five peaks which do not significantly change their position with the

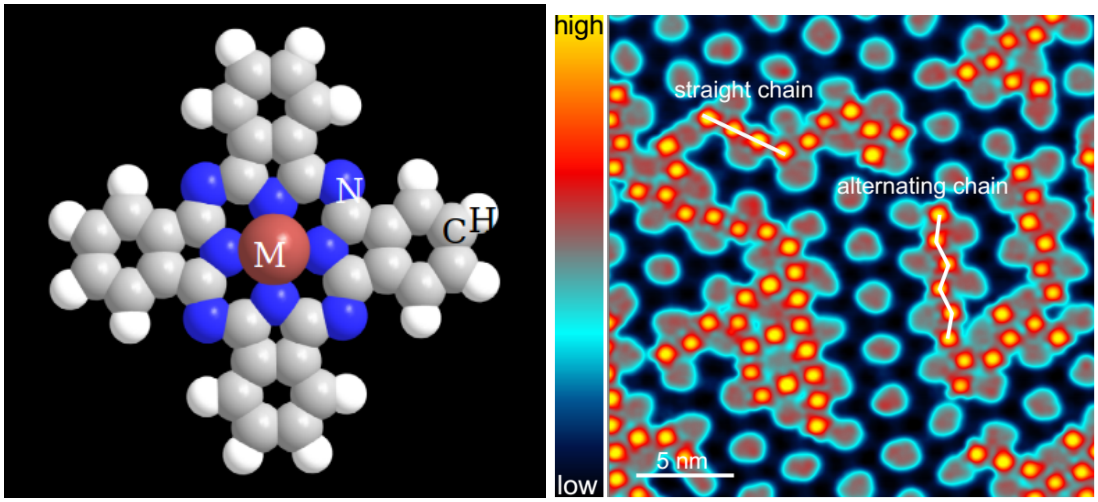

Figure 28: Left: Sketch of the metal-Phthalocyanine structure. Right: STM surface scan of the graphene layer and the sample. The color scheme illustrates the surface height showing the position of the sample molecules.

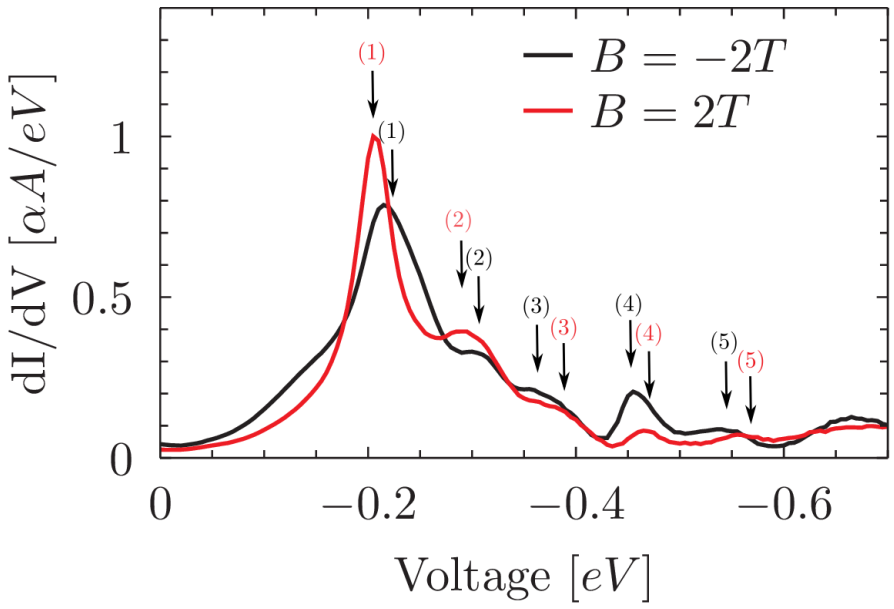

Figure 29: Experimental results for the differential conductance of Cobalt-Phthalocyanine as a function of the bias voltage between the STM tip and the substrate for two different magnetic fields.

reversal of the field direction. The peaks can be attributed to vibrational and electronic degrees of freedom. In contrast to setups with strongly hybridized molecules, an identification of the peaks and their position will give us information about the frequency of the dominating vibrational mode as well as the position of the electronic ground and first excited state. Switching the magnetic field leads to minor changes in the peak positions and significant changes in the shape and height of the peaks. For the positive field direction the first peak is sharp whereas for the negative field the height of the peak is reduced and a shoulder appears for low bias voltages. Opposite to this, the fourth peak is more pronounced for negative fields. The experiment therefore yields two novel results: The differential conductance, and thus energy spectrum, of the non-hybridized molecule and, simultaneously, a spin-resolved measurement of the conductance.

4.2. Model for spin-polarized magnetomechanical transport

The new experimental findings demand an explanation. Most of the parameters such as the energy spectrum of the molecule or the electron-phonon coupling are not directly accessible. The exact values of those parameters are not known and also can not be changed during the experiment. A theoretical model based on the experimental findings, however, creates the opportunity to access these parameters and yields the possibility to verify or disprove assumptions over the origin of the effects observed in the experimental data.

The molecule has both electronic and vibrational degrees of freedom and the former ones will in general include magnetic properties. To find a suitable Hamiltonian we establish a working hypothesis about the origin of the peaks found in the experiment (see Figure 29). The first (1) and the fourth peak (4) stand out due to their height and are therefore assumed to be of electronic origin. The remaining peaks which become successively smaller with increasing bias voltage are then of vibrational origin. This assumption is underlined by the equidistant peak positions hinting on one dominant molecular vibrational mode. Consequently, we formulate an Anderson-Holstein model [48, 49] to represent both the electronic and vibrational degrees of freedom of the sample molecule.

The full electronic spectrum of the molecule is rather complex and its calculation shall not be performed here. It is sufficient to realize that only a single electronic orbital is assumed to be relevant in the experiment. Hence, the electronic spectrum of the molecule is reduced to a single electronic level ϵ_0 similar to the quantum dot setup used in Chapter 3. Contrary to the previous model, however, a double occupation of

the electronic level is in principle possible. However, the energy of double occupation is increased by the electronic repulsion energy U. The quantum dot Hamiltonian reads

$$H_{\text{dot}} = \epsilon_0 \left(a_\uparrow^\dagger a_\uparrow + a_\downarrow^\dagger a_\downarrow \right) + U a_\uparrow^\dagger a_\uparrow a_\downarrow^\dagger a_\downarrow + \frac{g\mu_B}{\hbar} B s_z, \tag{38}$$

where a_σ is the annihilation operator for an electron with spin σ, U is the Coulomb repulsion between two electrons on the dot, s_z the electronic spin in z-direction and B the externally applied magnetic field. Just as before, μ_B and g denote the Bohr magneton and the g-factor, respectively. From the experimental results, we can extract the frequency of the dominant vibrational mode of $\omega \simeq 0.38eV$. The mode is coupled linearly to the electronic degrees of freedom according to

$$H_{ph} = \hbar\omega b^\dagger b + \lambda \left(b + b^\dagger \right) \sum_\sigma a_\sigma^\dagger a_\sigma, \tag{39}$$

with $b^\dagger$, b denoting the phonon annihilation and creation operators and the electron-phonon coupling strength λ. Both the STM tip and the substrate serve as electron reservoirs and will be modelled as ferromagnetic leads. The tip will be associated with the source lead and the substrate with the drain. In analogy with the experiment, the drain or substrate is a hard magnet and therefore has a fixed polarization direction in the positive z-direction. The source (or tip) polarization p_L is always aligned parallel to the external field B. Interaction between leads and sample is realized by the tunnel coupling Hamiltonians

$$H_{\text{tun,R}} = \sum_k \left[t_{kR} \left(a_\uparrow c_{k+}^\dagger + a_\downarrow c_{k-}^\dagger \right) + \text{h.c.} \right], \tag{40}$$

$$H_{\text{tun,L}} = \sum_k \left[t_{kL} \left(a_\uparrow c_{k\pm}^\dagger + a_\downarrow c_{k\mp}^\dagger \right) + \text{h.c.} \right], \tag{41}$$

for positive/negative external fields. The tunnel amplitude for lead α is given by $t_{k\alpha}$ and the annihilation operator for electrons in the leads with wavevector k and spin σ is given by $c_{k\sigma}$. The Hamiltonian for the leads reads

$$H_{\text{leads}} = \sum_{k\alpha} \left(\epsilon_{k\alpha} - \mu_\alpha \right) \left(c_{k\alpha+}^\dagger c_{k\alpha+} + c_{k\alpha-}^\dagger c_{k\alpha-} \right), \tag{42}$$

where $\epsilon_{k\alpha}$ is the energy for lead electrons with wavevector k and μ_α is the chemical potential of lead α which can be shifted by the bias voltage V_b. We choose a different

Eigenstate	Energy
$\|0\,n\rangle$	$\epsilon_{0n} = \hbar\omega n$
$\|\uparrow\, n\rangle$	$\epsilon_{\uparrow n} = \epsilon_0 - \lambda^2/\omega + B/2 + \hbar\omega n$
$\|\downarrow\, n\rangle$	$\epsilon_{\downarrow n} = \epsilon_0 - \lambda^2/\omega - B/2 + \hbar\omega n$
$\|d\,n\rangle$	$\epsilon_{dn} = 2(\epsilon_0 - \lambda^2/\omega) + U - 2\lambda^2/\omega + \hbar\omega n$

Table 2: Eigenstates and corresponding energies for the Anderson-Holstein Hamiltonian where n denotes the excitation of the phonon mode.

label for the bias voltage compared to the previous chapter to avoid confusion with the measurement units for the experimental data which is given in eV. In order to study the electron and spin dynamics, it is helpful to determine the energy spectrum of the system. The only off-diagonal term in the system Hamiltonian is the electron-phonon coupling. An analytic diagonalization is therefore possible using the polaron transformation. The unitary transformation is exactly the same as for the cooling model (see Eq.(32)). However, now we also get a shift in the energy for the doubly occupied quantum dot. The corresponding eigenenergies are given in Table 2.

4.3. Differential conductance and magnetomechanical molecular transport

Using the quantum master equation and the diagrammatic perturbation theory, we can now compare the experimental data to numerical calculations for our model. In order to stay as close to the experiment as possible, we use the same parameters for our numerical calculation as far as possible. The experiment is conducted at low temperatures of about $T = 6.5\text{K}$. This leads to an inverse temperature of $(k_\text{B}T)^{-1} = \beta = 178.51(\text{eV})^{-1}$. The external magnetic field has a local strength of $g\mu_B B = 2T = 0.12 \times 10^{-3}\text{eV}$. The magnitude of the tunnel coupling strength Γ can be estimated from the current values obtained in the experiment. A charge current of $I = 6.1\text{nA}$ indicates a tunnel coupling of $\hbar\Gamma \sim 0.6 \times 10^{-5} eV$. All other parameters can not be directly taken or measured from the experiment. The polaron-shifted energy of the electronic level $\bar{\epsilon} = \epsilon_0 - \lambda^2/\omega$, the Coulomb repulsion and the phonon frequency are contained in the peak positions of the differential conductance (see Figure 29). The strength of the electron-phonon coupling can then be estimated by fitting the theory results to the experimental curve. A comparison between the experimental and numerical data for the differential conductance as function of the applied bias voltage is shown for positive and negative values of the external magnetic field in Figure 30 and Figure 31, respectively.

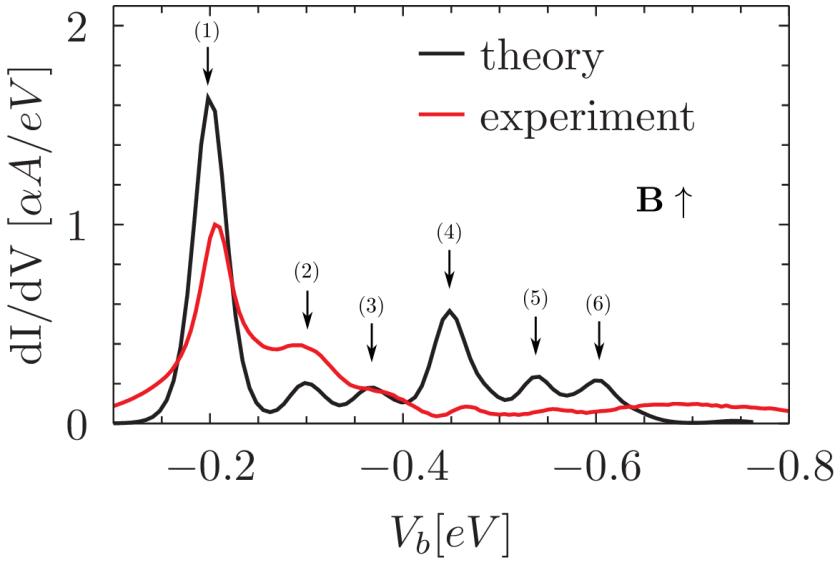

Figure 30: Comparison of the theoretical results and experimental data for the differential conductance as function of the bias voltage for positive magnetic field. The parameters are: $\epsilon_0 = 0.11\text{eV}$, $\Gamma_L = 10\Gamma_R = 3.5 \times 10^{-5}\text{eV}$, $g\mu_B B = 2\text{T}$, $\omega = 0.038\text{eV}$, $T = 6.5\text{K}$, $\lambda = 0.5\omega$, $p_L = 0.5$, $p_R = 0.95$ and $U = 0.15\text{eV}$.

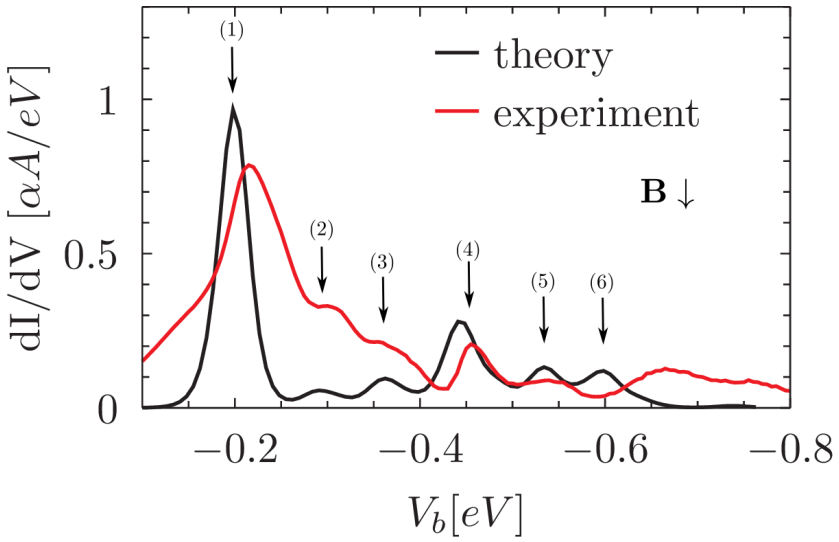

Figure 31: Comparison of the theoretical results and experimental data for the differential conductance as function of the bias voltage for negative magnetic field. The magnetic field value is $g\mu_B B = -2\text{T}$. The remaining parameters are the same as in Figure 30.

The numerical results for the theoretical model reproduce the main structure of the experimental data. We observe a series of peaks in the differential conductance with declining height for stronger bias voltages. This behaviour is interrupted by the fourth peak which is in the theory results significantly higher than the third. A similar behaviour can be found in the experimental data for negative external field. For positive magnetic fields, however, the fourth peak is much more pronounced in the theory than in the experiment. Additionally, a sixth peak is found in the numerical data which can not be clearly identified in the experiment. To judge about the quality of the agreement between the experimental and theoretical results, we should take into account the considerable reduction of the true setup to our simplified model with only a few parameters. Particularly the peak positions with respect to the bias voltage can be reproduced very well. The heights and lineshapes are not well reproduced.

Origin of the conductance peaks

Let us next identify the origin of the peaks by analyzing the energy spectrum of the Hamiltonian given in Table 2. The first peak (1) at around $-0.2eV$ can be attributed to an occupation of the quantum dot with a single electron. Notice that the external magnetic field induces a Zeeman splitting for the electronic spin and in principle leads to a double peak structure in the differential conductance. The Zeeman splitting however is directly proportional to the applied magnetic field and therefore several orders of magnitude smaller than most other energy scales in the problem. The signatures for both spin up and spin down electrons on the quantum dot therefore lie directly on top of each other and can not be distinguished. The second (2) and third peak (3) correspond to an occupation of higher vibrational states and are positioned at roughly -0.28eV and -0.36eV, respectively. The equidistant placing and the declining peak height indicate a vibrational origin and allow us to estimate the eigenfrequency of the vibrational mode in the experiment at $\omega \simeq 0.038eV$ as mentioned previously. Notice that the distance between the peaks in the differential conductance corresponds to twice the vibrational frequency since we plot the conductance against the bias voltage. In the numerical calculations, the bias voltage is applied symmetrically changing the chemical potential of the leads by $\mu_\alpha \pm eV_b/2$. This results in the additional factor of 2. By examining the energy spectrum we can associate the fourth peak (4) to a double occupation of the quantum dot. It is positioned at about -0.44eV which corresponds to the eigenenergy of the doubly occupied state with the vibrational mode in the ground state. The following fifth (5) and sixth peak (6) are then excitations of the higher vibrational states with

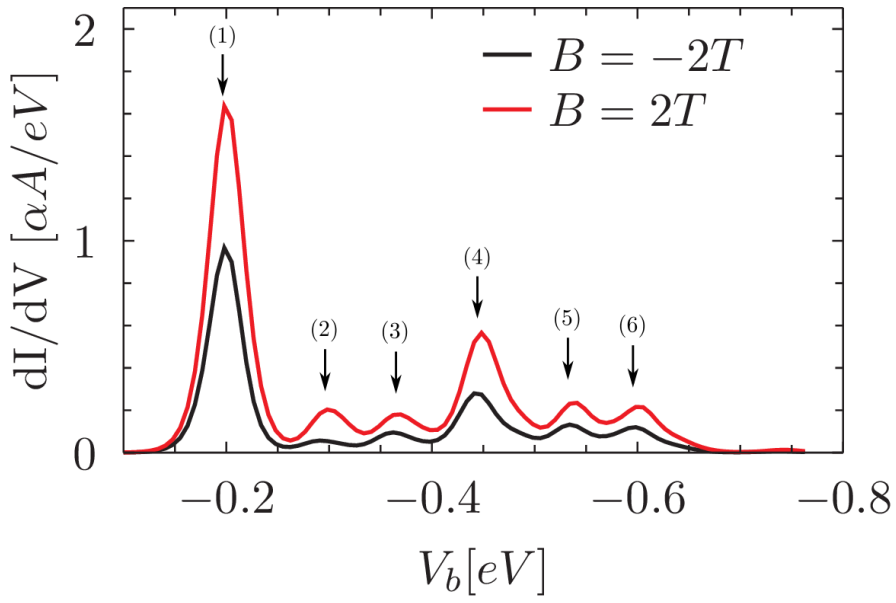

Figure 32: Theory results for the differential conductance dI/dV as a function of the applied bias voltage V_b for positive and negative magnetic fields. The parameters are the same as in Figure 30.

positions at about -0.52eV and -0.6eV. We are thus able to identify the origin of all peaks by excitation of electronic states and the corresponding vibrational sidebands. Not yet explained are the differences in the results for positive and negative magnetic fields.

In Figure 32, we compare the theoretical results for the differential conductance for positive and negative field values. The main difference between the two curves is an overall suppression of the current for negative magnetic fields. The source lead is a soft magnet which switches its polarization with the field direction. The drain lead however is modelled as a hard magnet with fixed polarization direction in the positive z-direction. Switching the external field into the negative z-direction therefore leads to an anti-parallel configuration of the ferromagnetic leads. The finite spin polarization of the leads in turn causes a spin blockade and thus reduces the overall current. In the experiment, however, (see Figure 29) a more complicated behaviour can be observed. Instead of a suppression of the current for negative fields we observe a change in the behaviour with increasing bias voltage. For low bias voltages the current is larger in the parallel configuration wheres at about -0.35eV the anti-parallel configuration

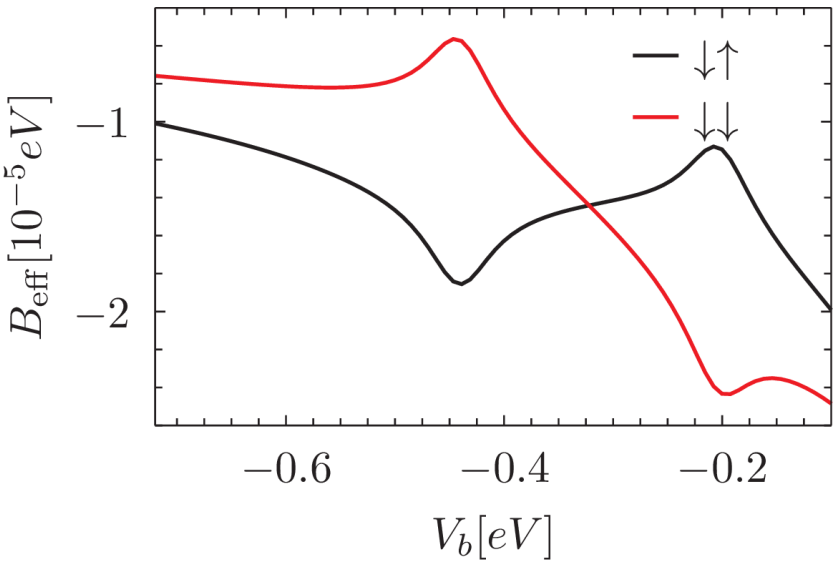

Figure 33: Effective field (see Eq.(43)) for the equilibrium phonon mode as function of the applied voltage. The parameters are the same as in Figure 30.

starts to overtake the parallel one. Experimental measurements of the current-voltage characteristics of the substrate without sample molecule indicate that the polarization of the substrate (drain lead) is not constant. Instead, it depends on the applied bias voltage. In the theory model, the absolute values of the lead polarizations are, however, fixed.

Finally we notice a slight shift in peak positions as well as the appearance of a shoulder or additional peak for low bias voltages in the experimental results. These features also can not be found in the numerical data.

4.4. Effective Field

The shift in the peak positions in the experimental results with a reversal of the magnetic field usually would indicate a change in the energy spectrum due to a Zeeman splitting. Moreover, we can observe a shift of the first peak towards larger bias voltages and a shift to weaker bias voltages for the fourth and fifth peak. The inversion of the effect for larger bias voltages corresponds to our observation regarding the peak heights. We assume that the non-monotonic behaviour is caused by a change in the lead polarizations. As previously discussed, however, the Zeeman splitting due to the external field is of the

order of 0.1meV and therefore several orders of magnitude smaller than the effects visible in the experimental data. In both the STM setup as well as the theory model, however, a second magnetic field appears which could lead to such effects. This field arises from the exchange interaction between the quantum dot and the ferromagnetic leads. The effects of this field induced by the ferromagnetic leads have been discussed in detail in [30, 31] and are summarized in Chapter 2.2.2. The references focus on the magnetic and electronic degrees of freedom and do not include vibrational effects in the models. The presence of a vibrational mode leads to a modification of the expression for the effective field compared to the analytic results given in Ref.[30]. Finding an analytic expression for the effective field in the presence of a non-equilibrium phonon mode proves a difficult task. If, however, the phonon mode is assumed to be at thermal equilibrium at all times, we find for the effective field

$$\boldsymbol{B}_{\text{eff}} = \sum_{\alpha=L,R} \frac{p_\alpha \Gamma_\alpha}{\pi} \left[\Omega(\epsilon_0 - \lambda^2/\omega) - \Omega(\epsilon_0 + U - 3\lambda^2/\omega)\right] \hat{n}_\alpha, \tag{43}$$

where $\hat{n}_\alpha$ denotes the unit vector of the polarization direction of lead α. The function $\Omega(E)$ results from the imaginary part of the Redfield rates and is given by

$$\Omega(\epsilon) = \frac{1}{2}\left[\Psi\left(\frac{1}{2} + \frac{i\beta}{2\pi}(\epsilon - \mu_\alpha)\right) + \Psi\left(\frac{1}{2} - \frac{i\beta}{2\pi}(\epsilon - \mu_\alpha)\right)\right] - \Psi\left(\frac{1}{2} + \frac{\beta E_c}{2\pi}\right), \tag{44}$$

where Ψ denote the digamma functions. A derivation of this expression can be found in the appendix. The expression for the effective field can be found by using diagrammatic perturbation theory to derive an equation for the dynamics of the electronic spin on the quantum dot [90]. A term for the rotation of the electron spin then appears which is induced by the effective field. It is well known that such an exchange field can be induced by the Coulomb interactions between the electrons. Notice that in the presence of the vibrational mode, it is possible to generate an attractive Coulomb interaction due to the polaronic shift of the electronic energies. In Figure 33 we show the effective field as a function of the applied bias voltage for the same parameters as in Figure 32. For the parallel lead configuration we find a peak in the effective field strength at around $-0.45eV$ and a local minimum at $-0.2eV$. For the anti-parallel configuration the local minimum and maximum are reversed. Notice that due to the asymmetric lead coupling the field is dominated by the drain lead (substrate). In Figure 34 we compare the effective field with the differential conductance. We observe that the local minimum and maximum of the field B_{eff} coincide with the two highest maxima in

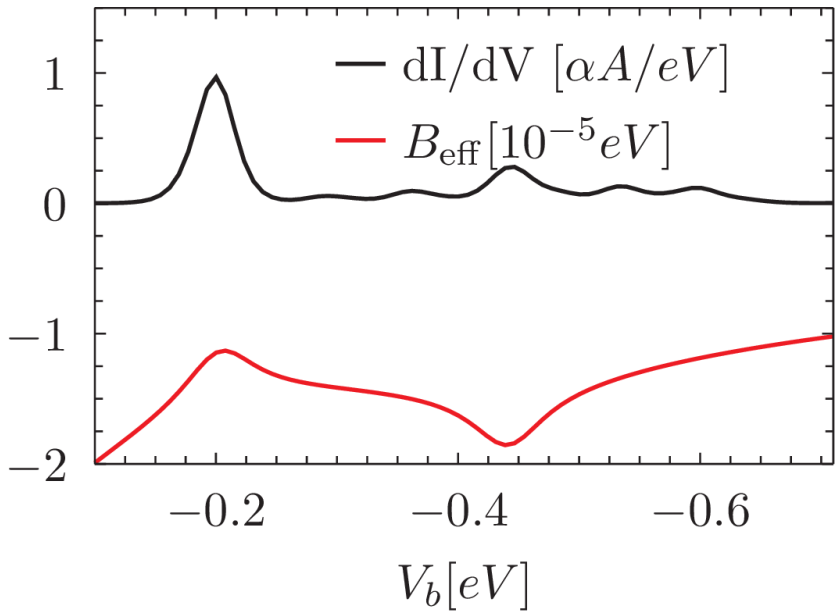

Figure 34: Comparison between the effective field and the differential conductance over the bias voltage for the parallel lead configuration. The parameters are the same as in Figure 30.

the differential conductance. As we have seen in Figure 33, reversing the source lead polarization exchanges the position of the local minimum and maximum of the effective field. In the experimental data given in Figure 29 a change in the ratio between the first and fourth peak can be observed in the differential conductance. The peak ratio shows the same qualitative behaviour as the extrema of the effective field. This effect however is not observed in the theoretical data shown in Figure 32. The reason lies in the size of the effective field in the numerical calculations. The strength of the effective field calculated from Eq.(43) using the same parameters as the numerical calculations is of the order of 10^{-5}eV. The magnitude of the effective field is mainly determined by the strength of the system-lead interaction Γ. The obtained values therefore coincide with the rough estimate of the experimental tunnel coupling used for the numerical calculation. Our estimation of the experimental parameter is based on the assumption of a single channel tunneling device. In such a case the maximum average current is given by one elementary charge times the tunneling coupling, $I \sim e\Gamma$. Due to the much more complicated experimental situation the measured current can strongly vary from this estimate. The relatively small value for the coupling strength in the numerical calculations is therefore chosen mainly due to the restrictions of the numerical procedure to sequential tunneling. Since the Redfield equation is only valid in the sequential tunneling limit we are not able to increase the coupling Γ unless we simultaneously increase the temperature of the system. The discrepancy between the theoretical and experimental results with respect to the direction of the external field could therefore originate in the different tunnel couplings. A numerical solution of the master equation including the next order in the tunnel couplings might yield further insight into the problem.

4.5. Non-equilibrium Phonon Mode

In the discussion of the effective field induced by the ferromagnetic leads, we have used an analytic expression which is based on the assumption of an equilibrium phonon mode. The numerical method used in this work, however, includes all non-equilibrium effects of the vibrational degrees of freedom to first order in the tunnel coupling. As we briefly discussed in Chapter 2.2.1, a common approach to phonon-assisted charge transport in nanosystems is to assume a thermal distribution of the phonon mode at all times. This assumption has the advantage that the vibrational degrees of freedom can then be integrated out, thereby effectively reducing the dimension of the density matrix. The disadvantage of this method is the loss of all information about the vibrational

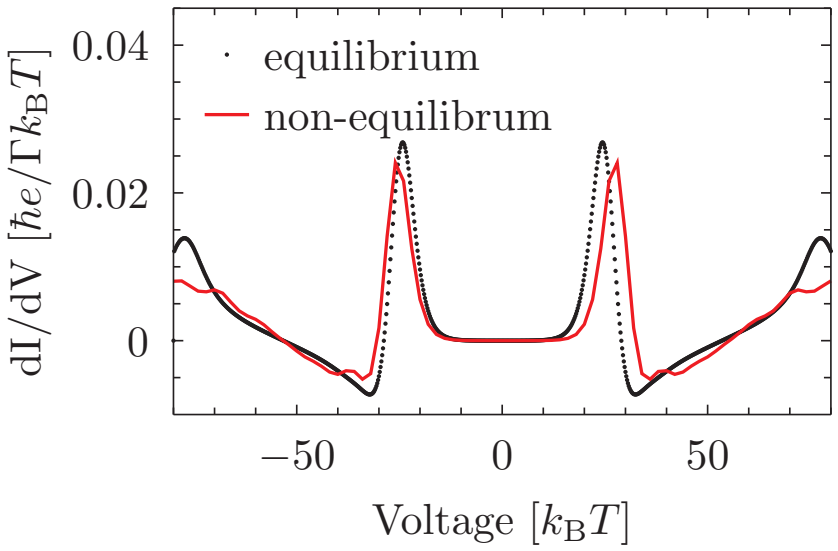

Figure 35: Comparison of the differential conductance as a function of the voltage for equilibrium (black data points) and non-equilibrium (red solid line) phonon mode. The parameters are: $\epsilon = 20k_BT$, $U = 30k_BT$, $B = 0$, $\omega = 5k_BT$, $\Gamma_L = \Gamma_R = 0.005k_BT$, $\lambda = 2.5k_BT$ and $p_L = p_R = 0.9$. The leads are polarized perpendicular to each other and perpendicular to the external field B.

degrees of freedom. In Chapter 3 we were interested in the average energy of the vibrational mode as a measure of the temperature. We were therefore forced to take into account the vibrational degrees of freedom explicitly. Consequently, it is not necessary to assume the vibrational mode to be at thermal equilibrium. In order to get a qualitative understanding of the difference between those two methods, we compare numerical data for both an equilibrium and a non-equilibrium phonon mode in Figure 35.

For low bias voltages, both results agree qualitatively and quantitatively. At around $V_b = \pm 25k_BT$ we observe a strong peak in the conductance corresponding the occupation of the electronic level ϵ_0. Here, both results agree qualitatively but small differences in the numerical data can be found. For larger bias voltages, we see qualitative differences between the two methods. The numerical calculations including non-equilibrium effects of the phonon mode show several small local maxima which can not be found in the data using the equilibrium distribution for the vibrational degrees of freedom. Finally, for large bias voltages, $V_b > 70k_BT$, a distinct difference between the two methods can be found. Determining the distance in between the small peaks in the non-equilibrium

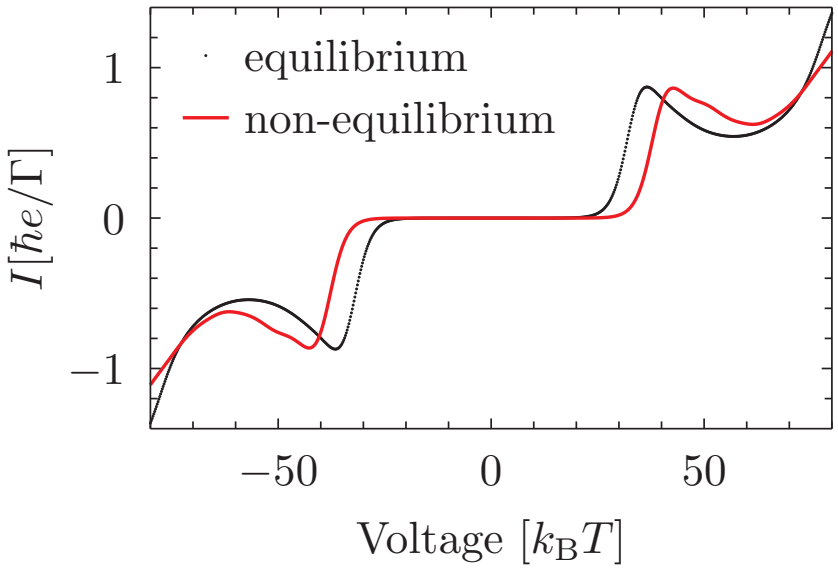

Figure 36: Comparison of the average charge current as a function of the bias voltage for equilibrium (black data points) and non-equilibrium (red solid line) phonon mode. The phonon frequency is $\omega = 5k_{\mathrm{B}}T$ and the electron-phonon coupling $\lambda = 4k_{\mathrm{B}}T$. The remainng parameters are the same as in Figure 35.

results shows that the peaks are separated by an energy which corresponds to twice the phonon frequency used for the calculation. We thus conclude that for small to intermediate bias voltages, $V_b < 50k_BT$, it is not necessary to consider non-equilibrium features of the vibrational mode. For larger bias voltages, however, additional structures appear in the differential conductance and an omission of non-equilibrium features leads to a loss of information even for the electronic degrees of freedom. The qualitative agreement between the two curves for bias voltages below $V_b = 50k_BT$ justifies our use of Eq.(43) for an estimate of the influence of the ferromagnetic leads on the quantum dot. A similar qualitative behaviour can be found in the current for stronger electron-phonon couplings as shown in Figure 36. For a general statement about the validity of the assumption of an equilibrium phonon mode, a more detailed comparison would be necessary. Especially the influence of stronger electron-phonon coupling λ or different temperatures T might play an important role. Here, the numerical calculations require a higher number of phonon states and therefore lead to longer calculation times especially for the non-equilibrium phonon mode. Recent calculations of the density of states of a vibrational quantum dot in the zero-temperature limit [91] agree with our observations. Using Monte-Carlo methods, Albrecht et. al find that the non-equilibrium distribution of the phonons becomes important with increasing bias voltages.

4.6. Conclusion

In this chapter, we have investigated the combined effects of ferromagnetically polarized leads and vibrational degrees of freedom on the transport through molecules. By using an Anderson-Holstein model to describe a scanning tunneling microscopy setup, we are able to recover most of the experimental features. A series of peaks in the differential conductance is found in both the experimental as well as the theoretical data. We identify the origin of the conductance peaks as a combination of electronic and vibrational states in the system and find a strong agreement between the peak positions in the experimental data and the numerical results. New experimental results are found by reversing the externally applied magnetic field and therefore changing the polarization of the STM tip. The changes in the peak intensities reported in the experiment can not be reproduced by our theoretical model. We compare the experimental data with an analytical expression for the effective magnetic field induced by the ferromagnetic leads. We find that, due to the numerical restriction to the sequential tunneling limit, the signatures of this effective field can not be observed in the theory model. The qualitative behaviour observed in the experiment, however, indicates a interaction of the

electronic spin on the molecule with the lead polarizations. We are therefore confident that a numerical calculation beyond the sequential tunneling limit will yield further insight into the experimental findings. Finally, a brief comparison between equilibrium and non-equilibrium features of the vibrational mode is made. Qualitative differences between the two numerical results can be found in the strong bias regime where a non-equilibrium distribution of the phonon mode leads to additional features in both the current and conductance. We conclude that the interplay between spin-polarized charge reservoirs and molecular vibrations yields interesting phenomena even in the absence of a direct magnetomechanical coupling.

5. Conclusion

In this thesis we have investigated the interplay of ferromagnetic polarization of leads with molecular vibrations. The interaction between electronic and mechanical degrees of freedom has been widely discussed in literature. Theoretical investigation have predicted the appearance of phonon blockades of the charge transport in both strong and weak coupling regimes which could be confirmed by experiments. The effect of spin-polarized charge transport through molecular devices has also received attention from both theoretical as well as experimental side. A combination of those two components however has not been explored up to now.

We focus on two different setups presented in Chapter 3 and Chapter 4. The first device is a magnetic quantum dot coupled to noncollinear ferromagnetic leads. We show that a polarization of the local magnetic moment of the quantum dot is possible by utilizing spin-polarized currents. The magnetization of the quantum dot can be used to achieve a cooling of the vibrational degrees of freedom in analogy to the macroscopic magnetocaloric demagnetization cooling. We have developed a proof-of principle model to determine the efficiency of the proposed cooling mechanism. The investigation of the spin and phonon dynamics for different orientations of the lead polarizations showed that an anti-parallel configuration of the source and drain lead polarization is optimal with respect to the cooling efficiency. Due to the different density of states in the ferromagnetic leads, a spin blockade of the charge current is formed which leads to an accumulation of spin on the quantum dot. The spin blockade reduces the inevitable Ohmic heating caused by the charge current and an accumulation of spin yields a fast and strong polarization of the local magnetic moment of the quantum dot. We find that the cooling effect induced by the magnetomechanical interactions then surpasses the Ohmic heating and a net cooling effect is achieved. A detailed investigation with respect to the different coupling parameters reveals the possibility to decrease the effective vibrational temperature of the nanodevice by 50% compared to its initial value. Additionally, we find an unexpected decrease of the cooling effect for stronger magnetomechanical couplings. Consequently, an efficient cooling setup can already be achieved for devices with weak to intermediate magnetomechanical couplings. This behaviour is demonstrated by a saturation of the cooling rate as a function of the magnetomechanical interaction. By reversing the lead polarizations, we are able to transform the cooling setup into a nanoheater. An investigation of asymmetric tunnel couplings to the leads shows that a dynamic cooling effect can also be achieved with a parallel configuration of

the lead polarizations. Here, we show that the effective vibrational temperature has a local minimum as a function of time. The asymmetric lead couplings lead to an increase of the cooling effect for short times which is then overcome by the Ohmic heating effect for longer times.

The second model we analyze is an Anderson-Holstein model coupled to ferromagnetic leads. In analogy to a recent experiment we determine the differential conductance of the Anderson dot. We find a strong agreement between the numerical and experimental data for the position of the peaks observed in the differential conductance. We determine that the observed structures originate from the occupation of vibronic and electronic states of the device. A difference between the theory model and the experimental observations is found when the externally applied magnetic field and the magnetization of the source lead are reversed. Here, the experimental data shows a change in the peak intensities which is not reproduced by the numerical calculations. An investigation of the effective magnetic field induced by the ferromagnetic leads shows that the strength of the magnetic interactions between leads and system is determined by the tunnel coupling. Unlike the experimental setup, the numerical calculations performed in this thesis are limited to the sequential tunneling limit which is valid only for weak system-lead couplings. Consequently, the tunnel coupling chosen for the numerical calculations is several orders of magnitude too small to observe a significant change in the differential conductance as result of a field reversal. Finally, we compare the influence of an equilibrium and a non-equilibrium phonon mode on the transport properties of the device. For small bias voltages we observe no qualitative changes in the charge current or conductance. At larger bias voltages, however, additional features appear in the presence of a non-equilibrium phonon mode.

In conclusion, we find that a combination of spin-polarized transport and vibrational degrees of freedom gives rise to interesting new phenomena. We show that, in the presence of direct magnetomechanical interactions, these effects can be used to manipulate the thermal energy of nanodevices. Furthermore, an influence of the electron-phonon interactions on the magnetic exchange field between the ferromagnetic leads and the device can be found even in the absence of a direct magnetomechanical coupling.

A. Integral Kernels

In this appendix we want to take a closer look at the diagrammtic expressions for the transition rates contained in the Redfield tensor. In Chapter 2.3.3 we have motivated the diagrammatic rules by deriving a corresponding expression (see Eq.(21)) for the double commutator appearing in Eq.(12). First, we determine the bath correlator $C_{k,\alpha}(t-t') = \langle B^\dagger_{k,\alpha}(t) B_{k,\alpha}(t')\rangle$. The bath correlator is given by the Fermi functions of the leads since the leads are modelled as non-interacting Fermi gases,

$$C_{k,\alpha}(t-t') = e^{-i\epsilon_k(t-t')} f^-_\alpha(\epsilon_k), \tag{45}$$

where $f^-_\alpha(\epsilon_k) = \left\{e^{(\epsilon_k-\mu_\alpha)\beta}+1\right\}$ denotes the Fermi function of lead α at temperature $T = 1/(k_\mathrm{B}\beta)$ and chemical potential μ_α. Next we assume the tunnel amplitude to be energy independent, $t_{k,\alpha} \to t_\alpha$. We can then transform the sum over the lead states in Eq.(21) into an energy integral, $\sum_k \to \int d\epsilon$. Introducing the tunnel coupling $\Gamma_\alpha = 2\pi|t_\alpha|^2$ then yields

$$\begin{aligned} &\textstyle\int_{-\infty}^t dt' \langle\varphi|H_{int}(t')W(t)H_{int}(t)|\varphi\rangle = \\ &= \textstyle\int_{-\infty}^t dt' \int d\epsilon \left[A^\dagger(t')A(t)\rho(t)f^+_\alpha(\epsilon)e^{i\epsilon(t-t')} + A(t')A^\dagger(t)\rho(t)f^-_\alpha(\epsilon)e^{-i\epsilon(t-t')}\right]. \end{aligned} \tag{46}$$

The next step is to perform the integrations over time and energy. First we introduce $\tau = t - t'$. Then we multiply by an infinitesimal factor $e^{-\eta\tau}$ with $\eta \to 0$. The time integral then is of the form

$$\int_0^\infty dx e^{-\eta x} e^{ix(A-B)} = \frac{i}{A-B+i\eta}. \tag{47}$$

Solving the time integral leaves an energy integration of the type

$$\Upsilon^\pm_\sigma(\epsilon) = \int_{-\infty}^\infty dE \frac{f^\pm_\alpha(E)}{\epsilon - E + i\sigma\eta}, \tag{48}$$

with $\sigma = +,-$. Due to the introduction of η the poles for the energy integration are now all lifted from the real axis. In order to make the integral convergent we introduce a Lorentzian cutoff $D_\alpha(E) = \frac{E_c^2}{(E-\mu_\alpha+iE_c)(E-\mu_\alpha-iE_c)}$. The integral can be solved by contour integration along half circles in the lower and upper complex plane with radius

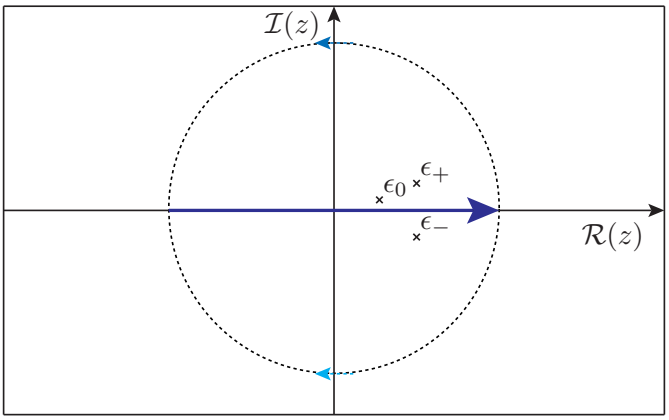

Figure 37: Integration contour in the complex plane.

$R \to \infty$ (see Figure 37). The functions has poles at

$$\epsilon_0 = \epsilon + i\sigma\eta, \qquad \epsilon_\pm = \mu_\alpha \pm iE_c, \qquad \epsilon_m = (2m+1)\frac{i\pi}{\beta} + \mu_\alpha. \tag{49}$$

The integrand vanishes on the half circles due to the infinite radius. A contour integration averaged over the upper and lower contour then yields

$$\begin{aligned}
\Upsilon^\pm_\sigma(\epsilon) \quad + \quad & i\pi\sigma D_\alpha(\epsilon) f^\pm_\alpha(\epsilon) = \\
= \quad & i\pi \left\{ \mp \frac{1}{\beta} \sum_{m=0}^{\infty} D_\alpha(\epsilon_m) \left(\frac{1}{\bar{\epsilon} - \bar{\epsilon}_m} - \frac{1}{\bar{\epsilon} + \bar{\epsilon}_m} \right) + \frac{D_\alpha(\epsilon)}{2} \left[\frac{\epsilon - \mu_\alpha}{2iE_c} \mp \tanh(\frac{i\beta}{2} E_c) \right] \right\} \\
= \quad & i\pi D_\alpha(\epsilon) \left[\frac{\epsilon - \mu_\alpha}{2iE_c} \mp \frac{1}{2} \tanh(\frac{i\beta}{2} E_c) \right] \\
\mp \quad & i\pi D_\alpha(\epsilon) \frac{1}{\beta} \sum_{m=0}^{\infty} \left(\frac{1}{\bar{\epsilon}_m - iE_c} + \frac{1}{\bar{\epsilon} - \bar{\epsilon}_m} + \frac{1}{\bar{\epsilon}_m - iE_c} - \frac{1}{\bar{\epsilon} + \bar{\epsilon}_m} \right) \\
= \quad & D_\alpha(\epsilon) \left[\frac{\pi}{2} \frac{\epsilon - \mu_\alpha}{E_c} \mp \frac{1}{2} \left\{ \Psi\left(\frac{1}{2} + \frac{i\beta}{2\pi} (\epsilon - \mu_\alpha) \right) + \Psi\left(\frac{1}{2} - \frac{i\beta}{2\pi} (\epsilon - \mu_\alpha) \right) \right\} \right. \\
\pm \quad & \left. \frac{1}{2} \left\{ \Psi\left(\frac{1}{2} + \frac{\beta E_c}{2\pi} \right) + \Psi\left(\frac{1}{2} - \frac{\beta E_c}{2\pi} \right) \right\} \right],
\end{aligned} \tag{50}$$

where we introduced $\epsilon - \mu = \bar{\epsilon}$. From the first to the second line we used

$$\begin{aligned} &D_\alpha(\epsilon_m)\left[\frac{1}{\bar{\epsilon}-\bar{\epsilon}_m}-\frac{1}{\bar{\epsilon}+\bar{\epsilon}_m}\right]= \\ &= D_\alpha(\epsilon)\left[\frac{1}{\bar{\epsilon}_m+iE_c}+\frac{1}{\bar{\epsilon}-\bar{\epsilon}_m}\right]+D_\alpha(\epsilon)\left[\frac{1}{\bar{\epsilon}_m-iE_c}-\frac{1}{\bar{\epsilon}+\bar{\epsilon}_m}\right]. \end{aligned} \tag{51}$$

And to evaluate the sums we exploit a property of the digamma function,

$$\begin{aligned} \frac{1}{\beta}\sum_{m=0}^{\infty}\left(\frac{1}{\bar{\epsilon}_m+iE_c}+\frac{1}{\bar{\epsilon}-\bar{\epsilon}_m}\right) &= \Psi\left(\frac{1}{2}+\frac{i\beta\bar{\epsilon}}{2\pi}\right)-\Psi\left(\frac{1}{2}+\frac{\beta E_c}{2\pi}\right), \\ \frac{1}{\beta}\sum_{m=0}^{\infty}\left(\frac{1}{\bar{\epsilon}_m-iE_c}-\frac{1}{\bar{\epsilon}+\bar{\epsilon}_m}\right) &= \Psi\left(\frac{1}{2}-\frac{i\beta\bar{\epsilon}}{2\pi}\right)-\Psi\left(\frac{1}{2}-\frac{\beta E_c}{2\pi}\right). \end{aligned} \tag{52}$$

The hyperbolic tangent can also be rewritten in terms of digamma functions:

$$\tanh\left(\frac{i\beta E_c}{2}\right)=\frac{1}{i\pi}\left[\Psi\left(\frac{1}{2}-\frac{\beta E_c}{2\pi}\right)-\Psi\left(\frac{1}{2}+\frac{\beta E_c}{2\pi}\right)\right]. \tag{53}$$

The cutoff energy is supposed to be large, thus enabling us to approximate (50) by

$$\boxed{\Upsilon^{\pm}_{\sigma}(\epsilon)\approx -\pi i\sigma f^{\pm}_{\alpha}(\epsilon)\mp\Omega(\epsilon),} \tag{54}$$

with

$$\Omega(\epsilon)=\frac{1}{2}\left[\Psi\left(\frac{1}{2}+\frac{i\beta}{2\pi}\left(\epsilon-\mu_\alpha\right)\right)+\Psi\left(\frac{1}{2}-\frac{i\beta}{2\pi}\left(\epsilon-\mu_\alpha\right)\right)\right]-\Psi\left(\frac{1}{2}+\frac{\beta E_c}{2\pi}\right). \tag{55}$$

All that remains in order to determine the analytic expression for the Redfield rates is to sum over all possible ingoing and outgoing states on the Keldysh contour and to insert the corresponding energies of the eigenspectrum of the system.

References

[1] G. Moore, Electronics **38** (1965).

[2] *Intel 22nm technology*, http://www.intel.com/content/www/us/en/silicon-innovations/intel-22nm-technology.html (2014).

[3] ITRS Edition Reports, http://public.itrs.net/reports.html (2010).

[4] S. Kubatkin, A. Danilov, M. Hjort, J. Cornil, J.-L. Brédas, N. Stuhr-Hansen, P. Hedegard, and T. Bjørnholm, Nature **425**, 698 (2003).

[5] H. Song, Y. Kim, Y. Jang, H. Jeong, M. A. Reed, and T. Lee, Nature **462**, 1039 (2009).

[6] Y. V. Nazarov and Y. M. Blanter, *Quantum Transport* (Cambridge University Press, 2009).

[7] S. Braig and K. Flensberg, Phys. Rev. B **68**, 205324 (2003).

[8] J. Koch and F. von Oppen, Phys. Rev. Lett. **94**, 206804 (2005).

[9] J. Koch, M. E. Raikh, and F. von Oppen, Phys. Rev. Lett. **95**, 056801 (2005).

[10] M. R. Wegewijs and K. C. Nowack, New J. Phys. **7**, 239 (2005).

[11] D. A. Ryndyk, M. Hartung, and G. Cuniberti, Phys. Rev. B **73**, 045420 (2006).

[12] F. Pistolesi and S. Labarthe, Phys. Rev. B **76**, 165317 (2007).

[13] J. Koch, M. Semmelhack, F. von Oppen, and A. Nitzan, Phys. Rev. B **73**, 155306 (2006).

[14] J. Koch, F. von Oppen, and A. V. Andreev, Phys. Rev. B **74**, 205438 (2006).

[15] K. Flensberg, Phys. Rev. B **68**, 205323 (2003).

[16] G. Steele, A. Hüttel, B. Witkamp, M. Poot, H. Meerwaldt, L. Kouwenhoven, and H. van der Zant, Science **325**, 1103 (2009).

[17] B. Lassagne, Y. Tarakanov, J. Kinaret, D. Garcia-Sanchez, and A. Bachtold, Science **325**, 1107 (2009).

[18] G. Weick, F. Pistolesi, E. Mariani, and F. von Oppen, Phys. Rev. B **81**, 121409 (2010).

[19] G. Weick, F. von Oppen, and F. Pistolesi, Phys. Rev. B **83**, 035420 (2011).

[20] J. Brüggemann, G. Weick, F. Pistolesi, and F. von Oppen, Phys. Rev. B **85**, 125441 (2012).

[21] G. Weick and D. M.-A. Meyer, Phys. Rev. B **84**, 125454 (2011).

[22] H. G. Craighead, Science **290**, 1532 (2000).

[23] C. Li, D. Zhang, X. Liu, S. Han, T. Tang, C. Zhou, W. Fan, J. Koehne, J. Han, M. Meyyappan, et al., Appl. Phys. Lett. **82**, 645 (2003).

[24] J. E. Green, J. Wook Choi, A. Boukai, Y. Bunimovich, E. Johnston-Halperin, E. DeIonno, Y. Luo, B. A. Sheriff, K. Xu, Y. Shik Shin, et al., Nature **445**, 414 (2007).

[25] F. Pistolesi, Y. Blanter, and I. Martin, Phys. Rev. B **78**, 085127 (2008).

[26] I. Zutic, J. Fabian, and S. D. Sarma, Rev. Mod. Phys. **76**, 323 (2004).

[27] J. König and J. Martinek, Phys. Rev. Lett. **90**, 166602 (2003).

[28] M. Braun, J. König, and J. Martinek, Phys. Rev. B **70**, 195345 (2004).

[29] M. Braun, J. König, and J. Martinek, Phys. Rev. B **74**, 075328 (2006).

[30] B. Sothmann, J. König, and A. Kadigrobov, Phys. Rev. B **82**, 205314 (2010).

[31] B. Sothmann and J. König, Phys. Rev. B **82**, 245319 (2010).

[32] A. L. Efros, E. I. Rashba, and M. Rosen, Phys. Rev. Lett. **87**, 206601 (2001).

[33] M. M. E. Baumgärtel, M. Hell, S. Das, and M. R. Wegewijs, Phys. Rev. Lett. **107**, 087202 (2011).

[34] G. E. W. Bauer, A. H. MacDonald, and S. Maekawa, Solid State Commun. **150**, 459 (2010).

[35] K. Uchida, S. Takahashi, K. Harii, J. Ieda, W. Koshibae, K. Ando, S. Maekawa, and E. Saitoh, Nature **455**, 778 (2008).

[36] F. Giazotto, T. T. Heikkilä, A. Luukanen, A. M. Savin, and J. P. Pekola, Rev. Mod. Phys. **78**, 217 (2012).

[37] J. T. Muhonen, M. Meschke, and J. P. Pekola, Rep. Prog. Phys. **75**, 046501 (2012).

[38] J. Brüggemann, S. Weiss, P. Nalbach, and M. Thorwart, Phys. Rev. Lett. **113**, 076602 (2014).

[39] P. Stadler, W. Belzig, and G. Rastelli, Phys. Rev. Lett. **113**, 047201 (2014).

[40] F. Pobell, *Matter and Methods at Low Temperatures* (Springer, Berlin, 2007).

[41] M. Ganzhorn, S. Klyatskaya, M. Ruben, and W. Wernsdorfer, Nature Nanotech. **8**, 165 (2013).

[42] O. Arcizet, V. Jacques, A. Siria, P. Poncharal, and P. Vincent, Nature Physics **7**, 879 (2011).

[43] S. Kolkowitz, A. C. B. Jayich, Q. P. Unterreithmeier, S. D. Bennett, P. Rabl, J. G. E. Harris, and M. D. Lukin, Science **335**, 1603 (2012).

[44] X. H. Qiu, G. V. Nazin, and W. Ho, Phys. Rev. Lett. **92**, 206102 (2004).

[45] J. Repp, G. Meyer, S. M. Stojkovic, A. Gourdon, and C. Joachim, Phys. Rev. Lett. **94**, 026803 (2005).

[46] M. Bazarnik, J. Brede, R. Decker, and R. Wiesendanger, ACS Nano **7**, 11341 (2013).

[47] F. Schulz, M. Ijäs, R. Drost, S. K. Hämäläinen, A. Harju, A. P. Seitsonen, and P. Liljeroth, Nature Physics **11**, 229 (2015).

[48] T. Holstein, Ann. Phys. **8**, 325 (1959).

[49] A. C. Hewson and D. Meyer, J. Phys.: Condes. Matter **10**, 196401 (2002).

[50] J. Kondo, Prog. Theor. Phys. **32**, 37 (1964).

[51] N. Makri and D. E. Makarov, J. Chem. Phys. **102**, 4600 (1995).

[52] N. Makri and D. E. Makarov, J. Chem. Phys. **102**, 4611 (1995).

[53] M. Thorwart, P. Reimann, P. Jung, and R. F. Fox, Chem. Phys. **235**, 61 (1998).

[54] P. Nalbach and M. Thorwart, Phys. Rev. Lett. **103**, 220401 (2009).

[55] R. P. Feynman and F. L. Vernon, Annals of Physics **24**, 118 (1963).

[56] X.-Q. Li, J. Luo, Y.-G. Yang, P. Cui, and Y. Yan, Phys. Rev. B **71**, 205304 (2005).

[57] J. König, J. Schmid, H. Schoeller, and G. Schön, Phys. Rev. B **54**, 16820 (1996).

[58] J. König, H. Schoeller, and G. Schön, Phys. Rev. Lett. **76**, 1715 (1996).

[59] A. Levy, R. Alicki, and R. Kosloff, Phys. Rev. E **85**, 061126 (2012).

[60] M. A. Reed, J. N. Randall, R. J. Aggarwal, R. J. Matyi, and T. M. Moore, Phys. Rev. Lett. **60**, 535 (1988).

[61] B. Weber, Y. H. M. Tan, S. Mahapatra, T. F. Watson, H. Ryu, R. Rahman, L. C. L. Hollenberg, G. Klimeck, and M. Y. Simmons, Nature Nanotechnology **9**, 430 (2014).

[62] S. Amaha, W. Izumida, T. Hatano, S. Tarucha, K. Kono, and K. Ono, Phys. Rev. B **89**, 085302 (2014).

[63] C. Timm and F. Elste, Phys. Rev. B **73**, 235304 (2006).

[64] F. Elste and C. Timm, Phys. Rev. B **73**, 235305 (2006).

[65] U. Weiss, *Quantum Dissipative Systems* (World Scientific, 2008).

[66] H. Bruus and K. Flensberg, *Introduction to Qauntum Field Theory in Condensed Matter Physics* (2001).

[67] C. Timm, Phys. Rev. B **77**, 195416 (2008).

[68] C. Mujica-Martinez, P. Nalbach, and M. Thorwart, Phys. Rev. E **88**, 062719 (2013).

[69] S. Weiss, J. Eckel, M. Thorwart, and R. Egger, Phys. Rev. B **77**, 195316 (2008).

[70] C. P. Slichter, *Principles of Magnetic Resonance* (Springer, 1990).

[71] Y. R. Shen, *The Principles of Nonlinear Optics* (Wiley, 1984).

[72] C. Cohen-Tannoudji, J. Dupont-Roc, and G. Grynberg, *Atom-Photon Interactions: Basic Processes and Applications* (Wiley, 1998).

[73] J. Jeske, D. Ing, M. B. Plenio, S. F. Huelga, and J. H. Cole, J. Chem. Phys. **142**, 064104 (2015).

[74] R. P. Feynman, Phys. Rev. **75**, 769 (1949).

[75] A. P. Jauho, *Introduction to the Keldysh nonequlibrium Green function technique* (2006).

[76] G. C. Wick, Phys. Rev. **80**, 268 (1950).

[77] F. Dyson, Phys. Rev. **75**, 1736 (1949).

[78] D. Rugar, R. Budakian, H. Mamin, and B. Chui, Nature **430**, 329 (2004).

[79] M. W. Zemansky, *Temperatures very low and very high* (Dover, New York, 1981).

[80] Y. Chen, C. Neill, P. Roushan, N. Leung, M. Fang, R. Barends, J. Kelly, B. Campbell, Z. Chen, B. Chiaro, et al., Phys. Rev. Lett. **113**, 220502 (2014).

[81] I. Bargatin and M. L. Roukes, Phys. Rev. Lett. **91**, 138302 (2003).

[82] P. Rabl, P. Cappellaro, M. V. G. Dutt, L. Jiang, J. R. Maze, and M. D. Lukin, Phys. Rev. B **79**, 041302 (2009).

[83] A. A. Kovalev, L. X. Hayden, G. E. W. Bauer, and Y. Tserkovnyak, Phys. Rev. Lett. **106**, 147203 (2011).

[84] A. Pályi, P. R. Struck, M. Rudner, K. Flensberg, and G. Burkard, Phys. Rev. Lett. **108**, 206811 (2012).

[85] J. Lehmann and D. Loss, Phys. Rev. B **73**, 045328 (2006).

[86] J. R. Schrieffer and P. A. Wolff, Phys. Rev. **149**, 491 (1966).

[87] I. G. Lang and Y. A. Firsov, Zh. Eksp. Teor. Fiz. **43**, 1843 (1962).

[88] P. A. M. Dirac, Proceedings of the Royal Society A **114**, 243 (1927).

[89] E. Fermi, *Nuclear Physics* (University of Chicago Press, 1950).

[90] S. Weiss, J. Brüggemann, and M. Thorwart, unpublished (2015).

[91] K. F. Albrecht, A. Martin-Rodero, J. Schachenmayer, and L. Mühlbacher, Phys. Rev. B **91**, 064305 (2015).

Danksagung

Im Folgenden möchte ich Prof. Dr. Michael Thorwart, Priv. Doz. Dr. Peter Nalbach und Dr. Stephan Weiss für ihre Anleitung, Beratung, Unterstützung und für ihre Geduld bei der Erstellung dieser Arbeit und der darin präsentierten Forschung danken. Des Weiteren bedanke ich mich für angeregte Diskussionen bei den Kollegen aus der Forschungsgruppe Thorwart. Finanziell wurde diese Arbeit unterstützt durch die Deutsche Forschungsgemeinschaft (DFG) als Teil des Schwerpunktprogrammes SPP 1538 "Spin Caloric Transport" und durch die Else-Heraeus Stiftung. Ich danke ausserdem meiner Familie, wo ich immer ein offenes Ohr für meine Probleme finden konnte.

Eidesstaatliche Versicherung

Hiermit erkläre ich an Eides statt, dass ich die vorliegende Dissertationsschrift selbst verfasst und keine anderen als die angegebenen Quellen und Hilfsmittel benutzt habe.

Hamburg, June 12, 2015 Jochen Brüggemann

Publikationsliste

J. Brüggemann, S. Weiss, P. Nalbach, and M. Thorwart, Phys. Rev. Lett. **113**, 076602 (2014), *Cooling a Magnetic Nanoisland by Spin-Polarized Currents*